Interleukin-1 receptor antagonist is a conserved early factor for exacerbating tuberculosis susceptibility

Ophelia V. Lee[1], Daisy X. Ji[2], Bruce A. Rosa[3], David L. Jaye[4], Sara Suliman[5], Makedonka Mitreva[3], Cem Gabay[6], Russell E. Vance[7]*, Dmitri I. Kotov[8]**

[1]Divison of Immunology and Molecular Medicine, University of California, Berkeley, Berkeley, CA, 94720, USA; [2]Department of Microbiology, New York University Grossman School of Medicine, New York, NY, 10016, USA; [3]Division of Infectious Diseases, Department of Medicine, Washington University School of Medicine, St. Louis, MO, 63110, USA; [4]Department of Pathology and Laboratory Medicine, Emory University, Atlanta, GA, 30322, USA; [5]Division of Experimental Medicine, Department of Medicine, University of California, San Francisco, San Francisco, CA, 94115, USA; [6]Division of Rheumatology, Department of Medicine, University Hospital of Geneva, Geneva, Switzerland; [7]Divison of Immunology and Molecular Medicine, Howard Hughes Medical Institute, University of California, Berkeley, Berkeley, CA, 94720, USA; [8]Division of Infectious Diseases, Department of Medicine, Andrew M. and Jane M. Bursky Center for Human Immunology and Immunotherapy Programs, Washington University School of Medicine, St. Louis, MO, 63110, USA.
*Correspondence: kotov@wustl.edu, rvance@berkeley.edu

Lead contact: Requests for further information and resources should be directed to and will be fulfilled by the lead contact, Dmitri I. Kotov (kotov@wustl.edu).

Summary

Mycobacterium tuberculosis (*Mtb*) causes 1.25 million deaths a year. However, tuberculosis (TB) pathogenesis remains poorly understood and is not fully recapitulated in standard mouse models. Here we find that gene signatures from three different *Mtb*-susceptible mouse models predict active TB disease in humans significantly better than a signature from resistant C57BL/6 (B6) mice. Conserved among susceptible mice, non-human primates, and humans, but largely absent from B6 mice, was *Mtb*-induced differentiation of macrophages into an *Spp1*$^{+}$ differentiation state. *Spp1*$^{+}$ macrophages expressed high levels of immunosuppressive molecules including IL-1 receptor antagonist (IL-1Ra). IL-1Ra was previously reported to cause *Mtb* susceptibility in one mouse model, but whether IL-1Ra is broadly important remains uncertain. Here we report that enhancement of IL-1 signaling via deletion of IL-Ra promoted bacterial control across three susceptible mouse models. We found IL-1 signaling amplified production of multiple cytokines by lymphoid and stromal cells, providing a multifactorial mechanism for how IL-1 promotes *Mtb* control. Our results indicate that myeloid cell expression of immunosuppressive molecules, in particular IL-1 receptor antagonist, is a conserved early mechanism limiting *Mtb* control in mice, non-human primates, and humans.

Keywords

Innate immunity, tuberculosis, IL-1 receptor antagonist, neutrophil, macrophage, osteopontin, Spp1.

Introduction

Mycobacterium tuberculosis (*Mtb*) causes ~10 million new cases of active tuberculosis (TB) disease and 1.25 million deaths per year, and is the leading cause of mortality from a bacterial pathogen[1]. Unfortunately, TB treatment consists of at least a 4-6 month regimen of antibiotics,

and the only approved vaccine has little to no efficacy in adults[2]. A greater understanding of the infection is essential, but this depends on tractable animal models that appropriately mimic *Mtb* pathogenesis in humans. While mouse models have led to key discoveries such as the critical role of IFN-γ[3,4] and TNF-α[5] in *Mtb* control, mouse models have also been criticized for not recapitulating key aspects of human disease, such as highly structured granuloma formation[6,7]. Further hallmarks of active tuberculosis (TB) disease in humans include expression of type I interferon (IFN) stimulated genes and a heightened neutrophil response[8,9]. The standard, resistant C57BL/6 (B6) mouse model only weakly exhibits these hallmarks[10–13].

We recently described *Sp140*$^{-/-}$ mice as an *Mtb*-susceptible mouse model that mimics the exacerbated type I IFN signature and heightened neutrophil response seen in humans[14,15]. *Sp140* encodes a transcriptional repressor that limits expression of the canonical type I IFN gene *Ifnb1*[16]. Loss of *Sp140* accounts for the excessive type I IFN response and *Mtb*-susceptibility of the previously described *Sst1*^{S} ("Kramink") mice[17–19]. Deletion of the gene encoding the type I IFN receptor (*Ifnar1*) rescues the hypersusceptibility of both *Sst1*^{S} and *Sp140*$^{-/-}$ mice, implying a causal role of type I IFNs in *Mtb* pathogenesis in these models[14,15]. Other *Mtb* susceptible mouse models have been described, such as *Nos2*$^{-/-}$ and *Acod1*$^{-/-}$ mice[20,21], though it remains unclear whether disease in these models is also driven by type I IFN signaling. Nevertheless, we hypothesized that there may be conserved features underlying the susceptibility of diverse mouse models, and that these features may be preserved across susceptible mice, non-human primates, and humans.

Neutrophilic inflammation is a major feature associated with tuberculosis disease across *Sp140*$^{-/-}$, *Nos2*$^{-/-}$, *Acod1*$^{-/-}$ and other susceptible mouse models[13,15,21–24], as well as during non-human primate[25,26] and human TB[27,28]. Depletion of neutrophils enhances bacterial control in diverse *Mtb*-susceptible mouse models, including *Sp140*$^{-/-}$, *Nos2*$^{-/-}$, and *Acod1*$^{-/-}$ mice[13,15,21]. However, the precise role of neutrophils in driving bacterial replication is unclear. One widely held view is that neutrophil necrosis and inflammation creates a replicative niche for the bacteria, including possibly within neutrophils themselves[29,30]. The production of neutrophil extracellular traps (NETs) is also speculated to promote bacterial replication, perhaps by induction of type I IFNs[15,22,31]. In states of chronic inflammation, neutrophils can also play immunosuppressive roles[32], though it remains uncertain if this accounts for neutrophil-driven exacerbation of TB disease[13,15,21].

Signaling induced by interleukin-1 (IL-1, comprising IL-1α and IL-1β) potently recruits neutrophils to sites of inflammation, and IL-1 is expressed at high levels in *Mtb*-susceptible mice[17,33] and humans[34]. Excessive IL-1 has been proposed to enhance bacterial replication[35], particularly in *Nos2*$^{-/-}$ mice[13,33], though the underlying mechanisms remain uncertain. A pro-bacterial function of IL-1 is difficult to reconcile with its clear anti-bacterial functions, as mice deficient in IL-1 signaling are highly susceptible to *Mtb* infection[23,36–40]. Importantly, the levels of IL-1 do not necessarily correlate with its signaling capacity. This is because IL-1 signaling is repressed by a decoy receptor (IL-1R2) and a soluble receptor antagonist (IL-1Ra, encoded by the *Il1rn* gene). Although susceptible *Sst1*^{S} mice express high levels of IL-1α and IL-1β, we previously reported that deficiency in *Il1rn* (resulting in enhanced IL-1 signaling) markedly promotes bacterial control in these mice[17]. These results imply that *Mtb*-susceptibility can arise from a lack of IL-1 signaling, rather than excessive IL-1 signaling, even when IL-1 levels are high. However, disease in *Sst1*^{S} mice may be a unique case since it is driven by an exacerbated type I IFN response[17], and *Il1rn* is an interferon-stimulated gene. Thus, it remains unclear whether impairment of IL-1 signaling by IL-1Ra plays a conserved role in humans or other *Mtb*-susceptible mouse models, especially *Nos2*$^{-/-}$ and *Acod1*$^{-/-}$ mice, in which *Mtb* infection is characterized by high levels of IL-1.

Here, in an effort to identify conserved mechanisms underlying *Mtb* susceptibility, we used single cell RNA sequencing (scRNA-seq) to profile and characterize three different *Mtb*-susceptible mouse strains (*Sp140*$^{-/-}$, *Nos2*$^{-/-}$, *Acod1*$^{-/-}$ mice). Unlike *Sp140*$^{-/-}$ mice, we found

that *Nos2*$^{-/-}$ and *Acod1*$^{-/-}$ mice did not exhibit a strong type I IFN signature and were not rescued by *Ifnar1* deficiency. Despite this, a common feature of *Mtb*-induced genes across all three strains was myeloid cell expression of immunosuppressive genes, such as *Arg1*, *Cd274*, and *Il18bp* (*Il1rn* is not in the *Mtb*-induced gene signatures because neutrophils were included in the naïve lung dataset and constitutively express *Il1rn*). In support of the importance of shared features of the *Mtb*-susceptible strains, gene signatures from each of these strains predicted human TB progression better than a signature obtained from resistant B6 mice. Additionally, macrophage differentiation into an *Spp1*$^{+}$ state was conserved across the susceptible mouse strains, *Mtb*-infected non-human primates, and *Mtb*-infected humans. Mouse, non-human primate, and human *Spp1*$^{+}$ macrophages expressed immunosuppressive molecules, including *Il1rn*. Given the importance of IL-1 signaling for *Mtb* control, and the strong expression of IL-1Ra in myeloid cells, we focused on the role of IL-1Ra in *Mtb* susceptibility. Global deletion as well as myeloid-specific deletion of IL-1Ra rescued bacterial control in *Sp140*$^{-/-}$ mice, demonstrating a major role for macrophage expression of this immunosuppressive molecule in driving *Mtb* disease. This contribution was shared across the susceptible mouse models, as global IL-1Ra deletion also enhanced bacterial control in *Nos2*$^{-/-}$ and *Acod1*$^{-/-}$ mice while neutrophil-specific IL-1Ra deletion did not, in line with macrophages being the dominant source of IL-1Ra during *Mtb* infection. Although *IL1RN* has been included in multiple human TB gene signatures[8,41–43], we find it alone was sufficient to strongly predict human TB and was induced early in the human response to TB with elevated levels detectable ~200 days prior to TB diagnosis. Together, these data suggest that immunosuppression by myeloid cells is a conserved feature of *Mtb* susceptibility across mice and humans, with some immunosuppressive pathways, such as IL-1 inhibition via IL-1Ra, being a shared early mechanism aggravating TB.

Results

Mtb-susceptible mice more accurately model human infection than B6 mice

Human *Mtb* infection presents as a highly diverse spectrum of diseased and non-diseased states. The best characterized hallmarks of active disease include induction of type I interferon (IFN) genes and a myeloid cell inflammatory response, especially by neutrophils[8]. We previously demonstrated that *Sp140*$^{-/-}$ mice exhibit both hallmarks, and that these hallmarks drive susceptibility in these mice[14,15]. Neutrophil trafficking to the lungs also promotes *Mtb* susceptibility in other mouse models[22,44–46], including *Nos2*$^{-/-}$ and *Acod1*$^{-/-}$ mice[13,21]. We sought to explore the use of different susceptible mouse models as a way to mimic the diversity of human TB disease. To start, we characterized the myeloid cell response in *Sp140*$^{-/-}$, *Nos2*$^{-/-}$, and *Acod1*$^{-/-}$ mice. We focused on ~4 weeks post-infection since it was an early timepoint where there were clear differences between resistant and susceptible strains. Although there are also major differences between strains at later timepoints, our rationale was to focus on earlier events to try to identify more proximal causes of susceptibility rather than indirect downstream consequences.

In line with previous reports, we observed a ~5-fold increase in lung neutrophils and a ~2-4-fold increase in lung monocytes and interstitial macrophages (IMs) in *Mtb*-susceptible mice 25 days after *Mtb* infection in each of the three mouse models (**Fig. 1A**). We sought to explore myeloid function in promoting *Mtb* susceptibility by first examining myeloid cell trafficking in *Mtb*-infected lungs from B6 and *Sp140*$^{-/-}$ mice (**Fig. 1B**). Diseased tissue within the lung was defined by the presence of *Mtb* and high cellularity. These features were largely absent from healthy portions of the lung. Diseased areas of the lungs had more macrophages (SIRPα^{+} cells) and neutrophils (Ly6G^{+} cells) than the healthy tissue of the same lungs (**Fig. 1C**). To confirm that this enrichment was not unique to *Sp140*$^{-/-}$ mice, we also compared macrophage and neutrophil

trafficking in B6, *Nos2*$^{-/-}$, and *Acod1*$^{-/-}$ mice (**Fig. 1D**). Similar to *Sp140*$^{-/-}$ mice, neutrophils were significantly enriched, and macrophages trended toward greater numbers in diseased relative to healthy tissue in all tested genotypes (**Fig. 1E**). Interestingly, while similar numbers of macrophages and neutrophils were recruited to the diseased portions of susceptible mouse lungs, macrophages were significantly closer to *Mtb* in B6, *Sp140*$^{-/-}$, *Nos2*$^{-/-}$, and *Acod1*$^{-/-}$ mice, as compared to neutrophils, which were more spatially segregated from *Mtb* (**Fig. 1F**). These data indicate that myeloid cells are more abundant in *Mtb*-infected lungs and preferentially traffic to sites of disease within those lungs, with macrophages residing closer to *Mtb* within the infected lung tissue.

As the heightened myeloid response was conserved across the *Mtb*-susceptible mouse models, we sought to test whether *Nos2*$^{-/-}$ and *Acod1*$^{-/-}$ mice share other attributes of the susceptibility of *Sp140*$^{-/-}$ mice, including type I IFN-driven disease. As myeloid cells are the primary reservoir of *Mtb*, we used our previously described single cell RNA-sequencing (scRNA-seq) workflow[15] to profile myeloid cells in *Mtb*-infected and naïve *Nos2*$^{-/-}$ and *Acod1*$^{-/-}$ mice. Infection with a fluorescent (wasabi^{+}) *Mtb* strain allowed us to distinguish infected and bystander cells in infected mice. The resulting datasets were integrated with our previously published B6 and *Sp140*$^{-/-}$ myeloid cell datasets[15] using the R package Seurat[47] (**Fig. 2A**). B6 mice were used as a control rather than *Sp140*$^{-/-}$ *Ifnar1*$^{-/-}$ mice because we previously demonstrated there is no difference in bacterial burden between these two genotypes 25 days post-infection (the timepoint of the scRNA-seq experiment)[14]. As these are CITE-seq[48] datasets, mRNA and protein expression of lineage and activation markers were implemented for the annotation of cell clusters (**Supplementary Fig. 1**). Comparing the myeloid cells from naïve lungs of B6, *Sp140*$^{-/-}$, *Nos2*$^{-/-}$, and *Acod1*$^{-/-}$ mice revealed very few differentially expressed genes between the mouse lines, suggesting that each genotype had a similar inflammatory state prior to infection (**Supplementary Fig. 1**). Therefore, differences between genotypes in *Mtb*-infected mice were likely induced in response to the infection rather than the result of pre-existing inflammation. Analysis of the myeloid cell clusters within the integrated dataset showed that the dominant myeloid cell populations (monocytes, macrophages, and neutrophils) are present in each genotype.

Given that the increase in neutrophils exhibited by *Mtb*-susceptible mouse models is a hallmark of human *Mtb* disease progression[27], we hypothesized that susceptible mouse models might mimic additional conserved hallmarks of active human disease, in which case they could be a useful tool to study *Mtb* pathogenesis. To test this hypothesis, we identified lung myeloid gene signatures consisting of genes induced at least 8-fold in *Mtb*-infected susceptible mice relative to naïve lungs (**Supplementary Figure 2**). The ability of these genes to discriminate *Mtb* cases from healthy controls in the TANDEM cohort[49] was quantified by calculating the area under the curve (AUC) for receiver operating characteristic (ROC) curves, with values closer to 1 indicating better classifiers of human disease (**Fig. 1B**). While there was no major difference in the ability of the signatures derived from the three susceptible mouse models to discern human disease, all the susceptible models considerably out-performed the signature derived from B6 mice, suggesting the susceptible mouse models better recapitulate characteristics of active human disease than B6 mice. We also tested the ability of these signatures to discriminate between active TB and latent TB-infected (LTBI) individuals in the Berry South Africa cohort[50], and similarly observed that the three susceptible mouse model signatures out-performed the B6 mouse signature, in line with the hypothesis that susceptible mouse models better recapitulate active human disease (**Fig. 1B**). The goal of this analysis was just to compare the immune response between mouse and human *Mtb* infection and was not to identify potential biomarkers of human *Mtb* infection. However, we also observed that the mouse signatures discriminated active TB infection from lung cancer and pneumonia in the Bloom et al. cohort[51], suggesting the similarity in immune responses between mice and humans

captured by these gene signatures does not solely reflect general inflammation (**Supplementary Figure 2**).

Next, we sought to better understand why the susceptible models were all able to discriminate between *Mtb* cases and healthy controls by assessing whether the type I IFN response present in humans[8] and *Sp140*$^{-/-}$ mice[14,15] was also present in *Nos2*$^{-/-}$ and *Acod1*$^{-/-}$ animals. Using our previously published gene signatures that distinguish between type I IFN and IFN-γ signaling[15], we classified cells as responding to type I IFN and/or IFN-γ in our myeloid scRNA-seq dataset. As expected, very few cells from naïve lungs were positive for either the type I or II IFN signature (**Fig. 2C**). Conversely, at least some *Mtb*-infected cells from every genotype had strong IFN-γ signaling, especially in monocytes and macrophages (**Fig. 2C, 2D**). However, the type I IFN response was notable only in the *Sp140*$^{-/-}$ mice, with strong type I IFN signaling in the neutrophils and interstitial macrophages (IMs) of these mice.

We experimentally tested whether type I IFN signaling plays a causative role in disease progression in each *Mtb*-susceptible mouse model by examining lung bacterial burden in *Ifnar1*-deficient *Sp140*$^{-/-}$, *Nos2*$^{-/-}$, and *Acod1*$^{-/-}$ mice 25 days after *Mtb* infection. As reported previously, global *Ifnar1*-deficiency fully rescued the susceptibility of *Sp140*$^{-/-}$ mice, phenocopying the *Mtb* restriction of B6 mice[14,15]; however, *Ifnar1*-deficiency only slightly reduced bacterial burdens in *Acod1*$^{-/-}$ mice and even modestly but not statistically significantly increased bacterial burdens in *Nos2*$^{-/-}$ mice (**Fig. 2E, 2F, 2G**). Together, these data suggest that while all three models recapitulate key aspects of human disease, there are major differences in the drivers of susceptibility between these mouse models.

Myeloid cell production of IL-1Ra is a conserved hallmark of Mtb susceptibility

As a strong type I IFN response was not shared among the three *Mtb*-susceptible mouse models, we analyzed our scRNA-seq to identify common features that may contribute to the elevated bacterial burdens present in these animals. We observed that *Mtb*-infection resulted in activation of the IMs, driving them to adopt either a proinflammatory *Trem2*$^{+}$ or an alternative *Spp1*$^{+}$ activation state[52–54] (**Fig. 3A, 3B**). A shift to *Spp1*$^{+}$ macrophage differentiation was recently associated with human tumor progression[54] and elevated plasma SPP1 levels correlate with active TB disease in humans[55]. Additionally, SPP1^{+} macrophages were present at an elevated frequency in bronchial alveolar lavage fluid from TB patients relative to LTBI individuals and healthy controls[56], and SPP1^{+} macrophages have been identified around granulomas in human lungs[57]. We therefore examined whether *Spp1*$^{+}$ macrophage differentiation correlated with *Mtb* susceptibility. Indeed, *Spp1*$^{+}$ macrophages were the dominant monocyte-derived macrophage population in the *Mtb*-susceptible *Sp140*$^{-/-}$, *Nos2*$^{-/-}$, and *Acod1*$^{-/-}$ mice, while being largely absent in *Mtb*-restrictive B6 mice (**Fig. 3C, 3D**). The *Spp1*$^{+}$ state was distinguished from the *Trem2*$^{+}$ state by the elevated expression of immunosuppressive molecules, including *Il1rn* (encoding IL-1Ra) which we previously demonstrated contributes to loss of bacterial control in *Mtb*-susceptible *Sst1*^{S} mice[17] (**Fig. 3E**). Alongside neutrophils, which constitutively express *Il1rn*[58], *Spp1*$^{+}$ IMs were the dominant source of *Il1rn* among myeloid cells and *Spp1*$^{+}$ IM *Il1rn* expression was elevated in all three susceptible strains relative to B6 mice (**Fig. 3F**). Reanalysis, including re-annotation, of a published scRNA-seq dataset of non-human primate *Mtb* granulomas indicated this expression pattern was conserved across species[59] (**Supplementary Figure 3**). SPP1^{+} macrophages were present in non-human primate *Mtb* granulomas, and the SPP1^{+} macrophages had higher expression levels of immunosuppressive molecules such as IDO1, CD274, IL18BP, and IL1RN than TREM2^{+} macrophages (**Fig. 3F, 3G**). Reanalysis and re-annotation of a scRNA-seq dataset of resected lungs from *Mtb*-infected humans also identified SPP1^{+} IMs with elevated expression of immunosuppressive molecules relative to TREM2^{+} IMs, including increased expression of IDO1, TGFβ, IL-10, IL-27, CD274, IL1RN, and the IL-1 decoy receptor IL1R2 (**Fig. 3I, 3J**). Additionally, SPP1^{+} IMs were a

dominant source of IL1RN among myeloid cells in the human lungs with the IL1RN-expressing SPP1$^+$ IMs present in metabolically active (FDG high signal) and metabolically inactive (FDG low signal) portions of *Mtb*-infected human lungs (**Fig. 3K**). Further examining the conserved nature of *Spp1*$^+$ macrophages, we identified a core *Spp1*$^+$ gene signature consisting of genes upregulated in *Spp1*$^+$ relative to *Trem2*$^+$ IMs in the three susceptible mouse models as well as in human *Mtb*-infected lungs. This core signature includes *IL1RN,* highlighting the strong association between *Spp1*$^+$ IM differentiation and *IL1RN* expression across species (**Supplementary Figure 4**).

Given the conserved nature of IL-1Ra expression, we tested whether *IL1RN* expression could discriminate between active *Mtb* cases and healthy controls in RNA-seq of PBMCs from the TANDEM cohort[49]. We observed high sensitivity and specificity for *IL1RN* alone (AUC=0.84) (**Fig. 3I**), which was only slightly improved by including *IL1RN* in a gene signature containing additional known immunosuppressive molecules, such as *IL18BP*[60], *CD274*[61], and *IL10*[62] (**Supplementary Fig. 5**). *IL1RN* alone was also highly discriminatory when discerning active TB versus LTBI cases when applied to the Berry South Africa dataset[50] (AUC=0.869; **Fig. 3M**). The high performance of *IL1RN* is consistent with prior work, as multiple published human TB signatures include *IL1RN*[8,41–43]. Analysis of *IL1RN* expression in the progressor population of the Adolescent Cohort Study[63] identified that increased *IL1RN* expression was detectable ~200 days before clinical TB diagnosis, in line with our hypothesis that IL-1Ra is an early mechanism of disease exacerbation (**Supplementary Fig. 5**). It is important to note that IFN response was the earliest detected transcriptional change in the Adolescent Cohort Study (observed ~12-18 months before diagnosis)[64], suggesting that other factors initiate loss of bacterial control which may then be amplified by immunosuppressive molecules including IL-1Ra. As IL-1 signaling is regulated by both IL-1Ra and the decoy IL-1R2 receptor, we also examined *Il1r2* expression in our scRNA-seq datasets and found lower *Il1r2* expression in *Mtb*-infected animals relative to naïve controls, suggesting *Il1r2* does not contribute to *Mtb* susceptibility (**Supplementary Fig. 5**). Taken together, our results indicate that myeloid cell expression of IL-1Ra is an important hallmark of early TB disease that is conserved across mice, non-human primates, and humans.

Spp1$^+$ *IM differentiation is unrelated to the M1 vs M2 macrophage differentiation paradigm*

Given the strong correlation between *Spp1*$^+$ macrophage differentiation, IL-1Ra expression, and *Mtb* disease progression, we sought to further examine the *Spp1*$^+$ IM response to *Mtb* infection, particularly in the case of the *Mtb*-susceptible *Sp140*$^{-/-}$, *Nos2*$^{-/-}$, and *Acod1*$^{-/-}$ mice. Our myeloid cell scRNA-seq dataset was used to determine potential markers for flow cytometric identification of *Spp1*$^+$ IMs and *Trem2*$^+$ IMs in infected mice. We found that *Itgax* (encoding CD11c) was upregulated on mature IMs, *Cd63* was preferentially expressed on *Trem2*$^+$ IMs, and *Cd9* was preferentially expressed by *Spp1*$^+$ IMs and was part of the core mouse *Spp1*$^+$ signature (**Fig. 4A, Supplementary Figure 4**). CD166, also known as Alcam, was recently identified as a marker of human *SPP1*$^+$ lung macrophages[65], while Trem2 and C1q are preferentially expressed by *TREM2*$^+$ lung macrophages in mice, non-human primates, and humans by scRNA-seq (**Fig. 3E, 3H, 3J**). Using a gating strategy to distinguish IMs from AMs, we then gated on the mature PD-L1^{hi} CD11c^{hi} IMs and used CD9 and CD63 as markers for *Spp1*$^+$ and *Trem2*$^+$ IMs, respectively (**Fig. 4B, Supplementary Figure 6**). CD9 and CD63 were validated as markers for these macrophage populations by assessing their staining for Alcam, Trem2, and C1q. As predicted, the CD9^{hi} *Spp1*$^+$ IMs stained brighter for Alcam while the CD63^{hi} *Trem2*$^+$ IMs stained brighter for Trem2 and C1q (**Fig. 4C**). We next assessed how *Mtb*-susceptibility impacts macrophage differentiation by comparing differentiation in B6, *Sp140*$^{-/-}$, *Nos2*$^{-/-}$, and *Acod1*$^{-/-}$ mice. Interestingly, all three susceptible mouse models displayed significant reductions in the frequency of mature IMs relative to B6 control mice, in line with the elevated monocyte recruitment observed in these animals following *Mtb* infection (**Fig. 1A, 4D**).

Of the mature IMs, there was a significant increase in *Spp1*$^{+}$ macrophage frequency in all three susceptible models, while *Trem2*$^{+}$ macrophage differentiation was reduced in *Nos2*$^{-/-}$ and *Acod1*$^{-/-}$ mice (**Fig. 4E, 4F**). These findings validate the scRNA-seq data and confirm that a shift from *Trem2*$^{+}$ to *Spp1*$^{+}$ IM differentiation correlates with loss of bacterial control (**Fig. 3D**).

As all three of the *Mtb*-susceptible mouse strains have increased bacterial burdens (**Fig. 2E, 2F, 2G**), we next asked whether *Mtb* infection directly drove *Spp1*$^{+}$ IM differentiation. Harboring *Mtb* correlated with an increase in *Spp1*$^{+}$ and *Trem2*$^{+}$ IMs by scRNA-seq and both populations exhibited higher rates of infection by flow cytometry when comparing *Sp140*$^{-/-}$ to B6 mice (**Fig. 4G, 4H**). However, the *Trem2*$^{+}$ IM were infected at a greater frequency than the *Spp1*$^{+}$ IM in B6 and *Sp140*$^{-/-}$ mice. Additionally, most cells of either IM subset were uninfected, suggesting direct infection is not a major driver of *Spp1*$^{+}$ IM differentiation. As differentiation into an M1 polarized state, marked by iNOS expression, or an M2 polarized state, marked by Arginase-1 (encoded by *Arg1*) expression, is a traditional view of macrophage differentiation, we tested whether *Trem2*$^{+}$ vs *Spp1*$^{+}$ differentiation mapped onto the M1 vs M2 paradigm. While Arg1 expression was largely restricted to the susceptible mouse models, iNOS and Arg1 were expressed by mature IMs, *Trem2*$^{+}$ IMs, and *Spp1*$^{+}$ IMs by scRNA-seq and flow cytometry demonstrating that *Trem2*$^{+}$ vs *Spp1*$^{+}$ differentiation is independent of canonical M1 vs M2 differentiation (**Fig. 4I, 4J**).

IL-1Ra is a conserved mediator of Mtb susceptibility

Next, we examined whether myeloid cell IL-1Ra expression plays a conserved role in amplifying *Mtb* disease. IL-1 is highly expressed in susceptible mouse strains[33], and has been hypothesized to contribute to the susceptibility of *Nos2*$^{-/-}$ mice to *Mtb*[13,33]. However, as we detected high levels of *Il1rn* expression in myeloid cells in *Sp140*$^{-/-}$, *Nos2*$^{-/-}$, and *Acod1*$^{-/-}$ mice, we hypothesized that perhaps IL-1 signaling was impaired in these mice despite the high levels of IL-1 cytokine. We hypothesized that perhaps the susceptibility of the mice was due to a functional deficiency in IL-1 signaling. In support of the inhibitory role of *Il1rn* during *Mtb* infection, global deletion of *Il1rn* in B6 mice slightly reduced lung bacterial burden (**Fig. 5A**). Neutrophils are major producers of *Il1rn* (**Fig. 3F**); however, neutrophils were not an obligatory source of *Il1rn*, as neutrophil-specific deletion of *Il1rn* using Mrp8^{Cre} *Il1rn*$^{fl/fl}$ mice had no effect on bacterial burden on the B6 genetic background (**Fig. 5B**).

We previously found that *Mtb*-infected *Sst1*^{S} mice exhibit high levels of IL-1 and yet bacterial burdens in these mice are rescued by enhancement of IL-1 signaling via deletion of *Il1rn*[17]. Likewise, we found that even heterozygous deficiency in *Il1rn* promotes bacterial control in *Sp140*$^{-/-}$ mice (**Fig. 5C**). However, as noted above (**Fig. 2**), *Sp140*$^{-/-}$ and *Sst1*^{S} mice exhibit a strong type I IFN signature that is largely absent from *Nos2*$^{-/-}$ and *Acod1*$^{-/-}$ mice. It was therefore of interest to test whether *Il1rn*-deficiency could also rescue bacterial burdens in *Nos2*$^{-/-}$ and *Acod1*$^{-/-}$ mice. We found that while deletion of one allele of *Il1rn* had no effect on *Mtb* control in *Acod1*$^{-/-}$ mice, complete deletion of *Il1rn* was sufficient to restore wild-type levels of bacterial control at day 25 post-infection (**Fig. 5D**). Interestingly, while bacterial burdens were reduced in *Acod1*$^{-/-}$ *Il1rn*$^{-/-}$ mice to levels seen in WT B6 mice, lung neutrophil numbers were still elevated in *Acod1*$^{-/-}$ *Il1rn*$^{-/-}$ mice (**Fig. 5E**). This result suggests that production of IL-Ra may be an important mechanism by which neutrophils drive *Mtb* susceptibility. However, neutrophil-specific deletion of *Il1rn* in *Acod1*$^{-/-}$ mice only slightly improved bacterial restriction, suggesting that while neutrophils may be a source of *Il1rn* during *Mtb* infection, they may not be the sole or dominant source (**Fig. 5F**). In two experiments with a higher and lower dose of *Mtb* inoculum, we also observed partial or complete rescue of bacterial burdens in *Nos2*$^{-/-}$ *Il1rn*$^{-/-}$ mice as compared to *Nos2*$^{-/-}$ mice (**Fig. 5G**). Similar to the *Acod1*$^{-/-}$ mice, no effect of *Ilr1rn* heterozygosity was observed, and the improved bacterial control in *Nos2*$^{-/-}$ *Il1rn*$^{-/-}$ mice did not coincide with a decrease in the number of lung neutrophils (**Fig. 5H**). Despite the increase in

neutrophils, neutrophil expression of *Il1rn* did not seem to be a major driver of the *Mtb* susceptibility for *Nos2*$^{-/-}$ mice, as neutrophil-specific deletion of *Il1rn* had no effect on bacterial control in these mice (**Fig. 5I**). These results demonstrate a conserved role for IL-1Ra in elevating *Mtb* burdens in three different mouse models at early infection timepoints, but do not rule out additional roles for IL-1Ra in suppressing immunopathology at later timepoints during TB (see Discussion).

The limited role for neutrophil production of IL-1Ra in the *Acod1*$^{-/-}$ and *Nos2*$^{-/-}$ mice is in line with prior reports which suggested that the secretion of IL-1Ra by neutrophils is relatively inefficient as compared to macrophages, and specific deletion of IL-1Ra in macrophages is protective during *Candida* infection[66]. Moreover, neutrophil expression of IL-1Ra is constitutive (including in resistant B6 mice) whereas it is induced in IMs (**Supplementary Figure 5**). Indeed, *Spp1*$^{+}$ IMs exhibited the highest expression levels of *Il1rn* among monocytes and macrophages and *Spp1*$^{+}$ IMs in all three susceptible mouse models expressed elevated levels of *Il1rn* relative to wild-type B6 controls (**Fig. 3F**). Additionally, macrophages localize closer to *Mtb* than neutrophils in all three susceptible mouse models (**Fig. 1F**). We therefore hypothesized that macrophage production of IL-1Ra could account for the conserved role of IL-1Ra in inhibiting bacterial control in *Mtb*-susceptible mice. To delete *Il1rn* in macrophages, we used CD64-Cre mice, which express Cre specifically in macrophages, at least in naïve animals[67]. Deletion of *Il1rn* in CD64^{Cre}*Il1rn*$^{fl/fl}$ mice[67,68] was able to rescue *Mtb* susceptibility of *Sp140*$^{-/-}$ mice (**Fig. 4F**). Together, these data reveal a conserved, myeloid cell role for IL-1Ra expression in exacerbating *Mtb* disease.

IL-1-enhanced cytokine and chemokine production promotes Mtb control

Given the conserved role for IL-1Ra in exacerbating early *Mtb* infection, we aimed to better define how IL-1 mediates protection against *Mtb*. We first examined IL-1R expression on myeloid cells, as they are the primary reservoir of *Mtb*, and found little to no expression of IL-1R in myeloid cells from naïve and *Mtb*-infected B6, *Sp140*$^{-/-}$, *Nos2*$^{-/-}$, and *Acod1*$^{-/-}$ mice (**Supplementary Fig. 7**). Consistent with a previous study[23], we also demonstrated that IL-1R-deficient macrophages do not exhibit a cell-intrinsic defect in bacterial control in mixed bone marrow (BM) chimera mice (**Supplementary Fig. 7**). It thus appears that IL-1 mediates its protective effect by signaling in bystander cells that then act non-cell autonomously to promote myeloid cell *Mtb* control. We therefore sought to identify the bystander cells that express IL-1R and the genes regulated by IL-1 in these cells to determine the mechanism by which IL-1 aids in bacterial restriction.

As IL-1 signaling in either hematopoietic or non-hematopoietic cells is sufficient for *Mtb* control early in infection[23,39], we sought to identify potential IL-1 responders in both compartments. Due to the inhibition of IL-1 signaling by high expression of IL-1Ra in the *Mtb*-susceptible mouse models, we used resistant B6 mice for examining IL-1 function. To ascertain the cell autonomous effects of IL-1, we generated mixed BM chimera mice with a 1:1 mix of WT and *Il1r1*$^{-/-}$ cells that were infected with *Mtb* following immune reconstitution (**Fig. 6A**). Among hematopoietic cells, IL-1 promotes cytokine expression in CD4^{+} T cells[69] and innate lymphoid cells (ILCs)[70,71]. In T cells, *Il1r1* was primarily expressed in T helper 17 cells (Th17) with some expression in Type 1 helper cells (Th1; **Fig. 6B, 6C, Supplementary Fig. 8**). Differential scRNA-seq gene expression profiling comparing WT and *Il1r1*$^{-/-}$ Th17 cells identified *Tnf*, *Gzmb*, and *Ifng* as genes with at least 2-fold greater expression in WT cells that were annotated as potential ligands in the NicheNet database[72] (**Fig. 6D**). Type 3 ILC (ILC3) and IL-17 producing natural killer T (NKT17) cells were the major *Il1r1*-expressing innate lymphoid cell populations in *Mtb*-infected lungs, with differential gene expression analysis identifying *Aimp1* and *Cxcl2* as potential IL-1-induced ligands produced by ILC3s; and *Tnf*, *Cxcl10*, *Itgb2*, *Il17a*,

Cxcl2, and *Rtn4* as potential IL-1-induced ligands produced by NKT17 cells (**Fig. 6E, 6F, 6G, Supplementary Fig. 8**).

Regarding potential non-hematopoietic sensors of IL-1, we first examined sensory neurons as they highly express IL-1R[73], and IL-1 signaling in neurons recruits myeloid cells[74]. As IL-1 signaling in hematopoietic cells is sufficient for early resistance to *Mtb* infection[23,39], we generated BM chimera mice that lacked hematopoietic IL-1R and either had IL-1 receptor in sensory neurons (CD45.1 and Adv$^{+/+}$ *Il1r1*$^{fl/fl}$ recipient mice) or not (Adv$^{cre/+}$ *Il1r1*$^{fl/fl}$ recipient mice). Sensory neuron-specific deletion of *Il1r1* had no effect on *Mtb* control, suggesting that other non-hematopoietic cells mediate the protective effect of IL-1 against *Mtb* (**Supplementary Fig. 7**). We thus performed scRNA-seq on BM chimera mice generated by transferring WT BM into lethally irradiated WT and *Il1r1*$^{-/-}$ hosts and then infected the chimeric mice with *Mtb* following immune reconstitution (**Fig. 6H**). Lineage markers used to annotate a scRNA-seq dataset of stromal cells in normal and hyperoxia-damaged murine lungs[75] were used to identify cell populations in our stromal cell scRNA-seq dataset (**Supplementary Fig. 8**). Based on this analysis, *Il1r1* was widely expressed in stromal cells, including in myofibroblasts, fibroblasts, and endothelial cells (**Fig. 6I, 6J**). Differential expression analysis of IL-1-regulated potential ligands, as annotated in NicheNet's database[72], identified *Icam1*, *Il6*, *Ccl2*, and *Wnt11* in myofibroblasts, *Cxcl1*, *Ccl2*, *Il6*, and *Cxcl9* in fibroblasts, and *Icam1* in endothelial cells as IL-1-induced potential ligands (**Fig. 6K**).

The most likely candidates for the protective effect of IL-1 signaling were then identified using NicheNet[72]. For this analysis, we focused on IMs as the receiver cells for the IL-1-regulated ligands, as IMs are known to harbor *Mtb* and control the infection[76]. According to the NicheNet ligand-receptor database, the receptors for IFN-γ, TNF, IL-6, CCL2, and IL-17 were expressed by IMs (**Supplementary Fig. 9**). While IFN-γ and TNF have well-established roles in *Mtb* control[3–5], the contribution of IL-17 has been appreciated more recently[77–80]. IL-22 is another cytokine important for bacterial control that is often co-produced with IL-17[81]. Thus, we tested whether IL-1-induced enhancement of IL-17/22 production was important in IL-1-mediated *Mtb* restriction. This hypothesis was tested by generating mixed BM chimera mice containing BM from *Il17*$^{-/-}$ *Il22*$^{-/-}$ and *Il1r1*$^{-/-}$ mice mixed at a 1:1 ratio as well as control mice (**Fig. 6L**). While the *Il17*$^{-/-}$ *Il22*$^{-/-}$: *Il1r1*$^{-/-}$ BM chimera mice contain cells that can respond to IL-1, as well as cells that can produce IL-17/22, no cell will be able to respond to IL-1 and express IL-17/22. Thus, these chimeras specifically eliminate the ability of IL-1 to amplify IL-17/22 production. The *Il17*$^{-/-}$ *Il22*$^{-/-}$: *Il1r1*$^{-/-}$ BM chimera mice were only slightly more susceptible than control animals, suggesting that an IL-1-mediated increase in IL-17/22 expression is not necessary for IL-1-driven protection (**Fig. 6M**). Therefore, we sought to identify which other potential ligands were the most likely drivers of IL-1-regulated *Mtb* restriction by IMs. We identified genes upregulated in activated IMs, and NicheNet[72] was then used to calculate the likelihood for each of the potential ligands to induce the transcriptional changes observed in the activated IMs. IFN-γ and TNF had the highest scores indicating they are the most likely candidates for how IL-1 protects against *Mtb*, while IL-17 had one of the lowest scores, in line with our experimental data (**Supplementary Fig. 9, Fig. 6M**). Taken together, these results suggest that IL-1-mediated protection against *Mtb* is multifactorial, involving responses by both hematopoietic and stromal cells that coordinate the activation of IMs by multiple anti-microbial cytokines.

Discussion

Mtb infection induces a chronic inflammatory state as evidenced by the induction of a type I/II IFN gene signature up to 12-18 months prior to disease diagnosis[27,64]. While aspects of this

inflammatory state—such as the IFN-γ response[3,4]—are vital for bacterial control, other components, such as the type I IFN response, exacerbate *Mtb* disease progression[8,15,22]. Our results lead us to hypothesize that the chronic inflammatory nature of *Mtb* infection may hinder bacterial control by promoting immunosuppression. We further propose that an underlying state of immunosuppression is conserved across susceptible mouse models, non-human primates and in humans. Within the cancer field, it has long been recognized that chronic inflammation supports cancer progression[82] with one major mechanism being the recruitment of so-called myeloid-derived suppressor cells (MDSC)[83]. MDSCs have also been proposed to exacerbate *Mtb* infection[22,84–87]. MDSCs are a heterogeneous population in mice and humans, with mouse MDSCs commonly identified based on Gr-1 antibody staining, which binds Ly6C and L6G, markers of monocytes and neutrophils, respectively[83]. While monocytes and neutrophils are commonly viewed as proinflammatory cells, MDSCs are immunosuppressive through multiple pathways, including via production of IL-10 and TGF-β[88]. During *Mtb* infection, monocytes and neutrophils are also heavily recruited to the lungs and specifically to sites of bacterial replication (**Fig. 1**).

In line with these findings, prior studies have described increased MDSCs in the blood of *Mtb*-infected individuals at frequencies similar to those found in human cancer patients[89] as well as increased lung MDSC frequency in non-human primates with active TB disease relative to latently infected animals[90]. Multiple pathways have been proposed for MDSC-driven immunosuppression of the host response against *Mtb* infection, including PD-1, IDO1, TGFβ, and IL-10[91,92]. For example, IDO1$^+$ PD-L1$^+$ myeloid cells reside in human granulomas and PD-L1 expression associates with active TB progression in humans[93]. However, the impact of immune suppression by myeloid cells on *Mtb* control is unclear, as highlighted by the contrasting results on the roles of PD-1 and IDO1 during *Mtb* infection. PD-1 deletion in mice and PD-1 blockade in rhesus macaques exacerbates TB disease[94,95], while IDO1 deletion does not change bacterial burden in mice[96] yet targeting IDO1 with a small molecular inhibitor promotes *Mtb* control in non-human primates[97,98]. Factors contributing to the lack of clarity for the role of immunosuppression during *Mtb* infection could be that not all immunosuppressive molecules may impact *Mtb* infection similarly and their effects may differ across models. For example, deletion or blockade of IL-10 has varying effects in mice depending on the genetic background and infection conditions[11,99–103]. Therefore, we applied a comparative approach to re-examine whether myeloid cells play an immunosuppressive role during *Mtb* infection, focusing on identifying conserved features of the myeloid cell response in *Mtb*-susceptible mice.

We first used scRNA-seq to characterize myeloid cells from *Mtb*-infected lungs of three *Mtb*-susceptible mouse strains that all exhibit neutrophil-driven disease, namely, *Sp140*$^{-/-}$, *Nos2*$^{-/-}$, and *Acod1*$^{-/-}$ mice[13–15,21]. Gene signatures derived from each of these mice significantly outperform wild-type B6 mice in their ability to discriminate human active *Mtb* cases from healthy controls or LTBI individuals, suggesting susceptible mice better mimic human disease. Due to the high predictive strength of all three models' gene signatures, it is likely that there are commonalities among the mouse models that are responsible for their discriminatory ability. These commonalities do not appear to be a general reflection of increased inflammation as these signatures could discriminate human active *Mtb* cases from lung cancer and pneumonia patients. Initially, we hypothesized that a likely candidate for a shared response to *Mtb* infection was type I IFN, as viral infections and the anti-viral type I IFN response correlate with the severity of *Mtb* disease in humans[8,64,104–106]. A functional role for type I IFNs in driving *Mtb* disease is also observed in mice, as inducers of type I IFNs exacerbate *Mtb* infection in B6 mice[36,107–112] and *Ifnar1* deletion rescues bacterial control in *Sst1*^{S} and *Sp140*-deficient mice[14,15,17]. To our surprise, however, a type I IFN signature was not conserved across susceptible mouse strains, and type I IFN receptor deletion had little to no effect on bacterial control in *Nos2*$^{-/-}$ and *Acod1*$^{-/-}$ mice (**Fig. 2**), indicating that other pathways drive their *Mtb* susceptibility.

As myeloid cells contribute to disease in each of the tested *Mtb* susceptible mouse models[13,15,21], we sought to define what pathways might be suppressed by myeloid cells to hinder *Mtb* control. We found that all three tested *Mtb*-susceptible mouse models had a shift in macrophage differentiation, exhibiting a reduction in *Trem2*$^+$ macrophages in favor of alternatively activated *Spp1*$^+$ macrophages. Interestingly, *Mtb*-restrictive B6 mice largely lacked *Spp1*$^+$ macrophages, and thus, *Spp1*$^+$ macrophage differentiation correlated with *Mtb*-susceptibility (**Fig. 3**). Macrophage differentiation into the SPP1$^+$ alternatively activated state also strongly correlates with tumor progression in humans[54]. Additionally, macrophage adoption of the SPP1$^+$ differentiation state was recently identified to be enhanced in the bronchial alveolar lavage fluid of active TB patients but not LTBI individuals or healthy controls[56] , and SPP1$^+$ macrophages were found to reside near human TB granulomas[57]. A commonality between *Mtb*-susceptible mice, human *Mtb* infection, and human cancer is the induction of a strong, chronic inflammatory state, raising the possibility that continued inflammation is a key driver of *Spp1*$^+$ macrophage differentiation. This concept is supported by the recent observation that SPP1$^+$ macrophages are associated with pathogenesis in individuals recently diagnosed with idiopathic pulmonary fibrosis, a disease with a median time to diagnosis of 2 years[65]. Additionally, SPP1$^+$ macrophage differentiation correlates with active rather than in remission Rheumatoid arthritis in humans[113]. Furthermore, SPP1 plasma levels were significantly higher in individuals with severe COVID-19 than those with mild/moderate COVID-19 or pneumonia[113] and SPP1 plasma levels correlate with human active TB disease[55].

As these reports correlating heightened inflammatory states with SPP1$^+$ macrophage differentiation are from human patients, it is challenging to understand the drivers of SPP1$^+$ differentiation. We, therefore, further characterized the macrophage response to *Mtb* infection in mice to better understand the mechanism underlying *Spp1*$^+$ differentiation. As part of this work, we identified CD9 and CD63 as markers that can be used for flow cytometry to distinguish mouse *Spp1*$^+$ from *Trem2*$^+$ macrophages (**Fig. 4**). Using these markers, we recapitulated our scRNA-seq data demonstrating a shift from *Trem2*$^+$ to *Spp1*$^+$ differentiation in all three susceptible mouse models relative to B6 mice. With this flow cytometry-based assay, we were able to demonstrate that direct infection by *Mtb* is not required for *Spp1*$^+$ differentiation and in fact *Trem2*$^+$ macrophages are infected at a higher rate than *Spp1*$^+$ macrophages. Additionally, we found that *Spp1*$^+$ versus *Trem2*$^+$ differentiation does not map onto the classic M1 versus M2 paradigm with both populations expressing canonical markers of M1 and M2 differentiation (e.g. iNOS and Arg1). While we have ruled out potential drivers of *Spp1*$^+$ differentiation, such as direct *Mtb* infection, further work is needed to identify the pathway or pathways promoting *Spp1*$^+$ macrophage differentiation. Nevertheless, *Spp1*$^+$ macrophages may play a key role in the early exacerbation of *Mtb* disease as they are the dominant macrophage source of IL-1Ra in mice. This expression pattern is conserved across species as we find SPP1$^+$ macrophages are also present in *Mtb* lung granulomas in non-human primates and humans and upregulate several immunosuppressive molecules relative to TREM2$^+$ macrophages, including *IL1RN* (**Fig. 3**). It should be noted that *Spp1*$^+$ differentiation appears to occur in response to strong inflammatory environments. Therefore, *Spp1*$^+$ macrophage differentiation and their IL-1Ra production is likely not the first step in TB progression but instead part of a positive feedback loop that accelerates progression, potentially in only a subset of human patients. Indeed, we observed that elevated *IL1RN* expression was detectable ~200 days prior to clinical diagnosis of TB in the Adolescent Cohort Study (**Supplementary Fig. 5**), suggesting that *IL1RN* is an early mechanism furthering human TB disease; however, it is not the initial trigger for loss of bacterial control as type I interferon responses are detectable 12-18 months prior to diagnosis in the same cohort[64]. The correlation between *Mtb* susceptibility and elevated IL-1Ra expression by macrophages was particularly intriguing as IL-1 signaling is a critical pathway for *Mtb* control[23,36–39].

However, the role of IL-1 during *Mtb* pathogenesis has been confusing. Mice deficient in IL-1 signaling are clearly susceptible to *Mtb*[23,36–40], but at the same time, many susceptible

mouse models exhibit elevated levels of IL-1[17,33], leading some to propose that IL-1-driven neutrophilic inflammation actually exacerbates *Mtb*[13,29]. Here we propose that the apparently paradoxical effects of IL-1 can be rationalized by an appreciation that high levels of IL-1 cytokine do not necessarily imply high levels of IL-1 signaling. Indeed, the beneficial effects of IL-1 can be counteracted by high levels of the decoys IL-1R2 or IL-1Ra[114]. In addition to *Spp1*$^{+}$ macrophage expression of *Il1rn* (encoding IL-1Ra), our scRNA-seq data indicated that *Il1rn* was constitutively expressed by neutrophils, as has also been shown for human neutrophils[58] (**Fig. 3**). Despite strong expression of *Il1rn* by neutrophils, neutrophils secreted considerably less IL-1Ra than monocytes upon stimulation and macrophage-specific deletion of *Il1rn* restored control of *Candida* infection[66]. Similarly, we found that expression of IL-1Ra by CD64^{+} cells, such as macrophages, is specifically required for *Mtb* control as CD64-Cre-mediated deletion of *Il1rn* was sufficient to rescue the susceptibility of *Sp140*$^{-/-}$ mice. This result correlates with human disease as macrophages are one of the primary IL-1Ra-expressing cell types in human *Mtb* granulomas[115].

Given the high levels of IL-1Ra expression by IMs in the susceptible mouse models, we predicted that IL-1Ra adversely affects *Mtb* control in each of the susceptible lines, which was confirmed by rescuing bacterial control in all three mouse lines with global deletion of IL-1Ra. Further implicating macrophages as the dominant source of IL-1Ra during *Mtb* infection, neutrophil-specific deletion of *Il1rn* resulted in little to no improvement in bacterial control in *Acod1*$^{-/-}$ and *Nos2*$^{-/-}$ mice. This result aligns with our imaging data, as macrophages were located significantly closer to *Mtb* than neutrophils in the diseased portion of the lungs of all three susceptible mouse strains. However, the finding that global *Il1rn* deletion partially rescues *Nos2*$^{-/-}$ mouse susceptibility was highly unexpected given prior claims that excessive IL-1 signaling is detrimental during *Mtb* infection[35] , particularly following the onset of the adaptive immune response in *Nos2*$^{-/-}$ mice[13,33]. Our results instead suggest that the initial lack of bacterial control in highly inflamed *Mtb*-susceptible mouse models, such as *Acod1*$^{-/-}$ and *Nos2*$^{-/-}$ mice, is primarily due to insufficient rather than excessive IL-1 signaling. Our results are in line with the susceptibility of mice deficient in IL-1 signaling[23,36,38,39], as well as with anecdotal evidence in humans reporting *Mtb* reactivation following IL-1Ra (Anakinra) treatment[116].

Importantly, our study focused on assessing bacterial burdens at a relatively early timepoint after infection (day 25) and do not exclude the possibility that excessive IL-1 signaling at later timepoints might have additional detrimental effects[117]. In particular, while IL-1 might be important for orchestrating bacterial control, it is also well-known to mediate significant immunopathology. This balance is exhibited in our previous work in which deletion of *Il1rn* completely rescued bacterial control in *Sst1*^{S} mice early in infection but resulted in only a minor improvement in survival, while deletion of a single allele of *Il1rn* nearly phenocopied the survival of *Mtb*-restrictive B6 mice[17]. It thus remains unclear whether IL-1 signaling could be manipulated therapeutically during human TB. Indeed, although myeloid cell production of IL-1Ra impairs bacterial control, IL-1Ra expression likely evolved to limit host pathology and therefore may be beneficial in many cases. Additionally, IL-1Ra is likely just one of many molecules that dictate the balance between bacterial control and host pathology during *Mtb* infection. For example, our gene signatures for the *Mtb*-susceptible mouse lines (but not the *Mtb*-restrictive B6 mice) contain other known immunosuppressive molecules, such as *Cd274* and *Il18bp*. Overall, our results therefore suggest that host-directed therapy to *Mtb* may require a delicate balance between anti-bacterial and host-tolerance mechanisms.

The mechanism by which IL-1 exerts its protective effects remains the subject of intensive study. In line with the limited expression of *Il1r1* by infected myeloid cells in our scRNA-seq dataset, IL-1 has been proposed to act on uninfected bystander cells that then promote myeloid cell *Mtb* control[23,39]. IL-1 signaling in either hematopoietic or non-hematopoietic bystander cells is sufficient to mediate protection during early infection[23,39]. Yet the mechanism for IL-1-mediated protection is not fully established, with eicosanoid regulation and synergistic

interactions between IL-1 and TNF being two potential mechanisms[36,39]. Our BM chimera scRNA-seq experiments suggest that a lack of a single simple mechanism is due to the complex and multifactorial effects of IL-1 on multiple cell types. We identified multiple IL-1-induced cytokines and chemokines as potential activators of *Mtb*-harboring IMs, with the most likely being *Ifng* and *Tnf*, two cytokines known to play a key role in *Mtb* restriction[3–5]. As IL-1 signaling in $CD4^+$ T cells directly promotes cytokine production[69], it is likely that IL-1 directly enhances *Ifng* and *Tnf* production by T cells and ILCs throughout *Mtb* infection. We hypothesize that IL-1-enhanced *Ifng* and *Tnf* production by $CD4^+$ T cells likely then act on *Mtb*-harboring IMs to promote their restriction of the infection. It is also possible that IL-1, potentially by promoting *Ifng* and *Tnf*, modulates hematopoiesis thereby impacting *Mtb* control. This hypothesis is supported by recent work demonstrating that the heightened type I interferon response in mice deficient in *Il1r1* drives a shift in their hematopoiesis as well as their enhanced *Mtb* susceptibility[9]. During *Legionella pneumophila* infection, IL-1 acts on type II alveolar epithelial cells inducing their expression of GM-CSF[118], another cytokine that activates macrophages with an established contribution to *Mtb* control[119–121]. Our stromal scRNA-seq dataset had limited coverage of epithelial cells so we were unable to observe whether IL-1 also induces GM-CSF expression in type II alveolar cells during *Mtb* infection. However, it is likely that this mechanism is conserved between *Legionella* and *Mtb* infections given the critical role played by GM-CSF and stromal cell IL-1 signaling in both infections.

In summary, our data support a model in which initial loss of bacterial control, whether due to a type I IFN response, *Nos2*-, or *Acod1*-deficiency, results in myeloid cell influx into *Mtb*-infected lungs. The incoming monocytes differentiate into IMs that adopt the *Spp1*$^+$ activation state in animals with heightened inflammation, which correlates with the upregulation of IL-1Ra. This high level of IL-1Ra expression hinders critical IL-1 signaling in hematopoietic and non-hematopoietic cells, reducing the production of *Mtb*-restrictive cytokines, such as TNF and IFN-γ. The IL-1Ra-mediated blockade of IL-1 thus generates an early positive feedback loop promoting bacterial replication in which *Mtb*-harboring myeloid cells are unable to restrict the bacteria. Enhanced bacterial replication leads to the influx of yet more myeloid cells and further increases IL-1Ra levels. While intervention abolishing this early feedback loop (e.g. IL-1Ra blockade) may temporarily promote bacterial control, the long-term cost of such an intervention would likely be an increased risk of immunopathology as this intervention would not address the initial insult that rendered the individual susceptible to TB, such as a strong type I IFN response. Our results are largely consistent with a recently proposed ‘tipping-point’ model of tuberculosis[122], which suggests that neutrophils cause a feedforward loop exacerbating disease even if they are not the initial driver of loss of *Mtb* restriction. In this study, we provide molecular evidence for this model by elucidating key molecular and cellular players that orchestrate the tipping point.

Acknowledgments

We thank members of the Vance, Barton, Stanley, and Cox laboratories for advice and discussions; the Stanley and Cox labs, and in particular D. Fox, for the shared operation of the UC Berkeley BSL-3 and ABSL-3 labs; S. Gupta and P. Khatri for advice on analysis of human cohorts; B. Malissen, S. Khader, and Y. Belkaid for mice; P. Dietzen, R. Chavez, J. Morales, and J. Rodriguez for technical assistance; A. Valeros, H. Nolla, and K. Heydari of the UC Berkeley Cancer Research Laboratory Flow Cytometry facility for assistance with flow cytometry; H. Aaron and F. Ives of the UC Berkeley Cancer Research Laboratory Molecular Imaging Center (RRID:SCR_017852) for assistance with confocal microscopy (supported by the Helen Wills Neuroscience Institute). Model figures were created with BioRender.com. D.I.K. is supported by an NIH Postdoctoral Fellowship (F32HL158250). C.G. is supported by the Swiss

National Science Foundation (310030B_201269) and the Rheumasearch Foundation. S.S. is supported by the NIH grant R01AI175614. R.E.V. is an Investigator of the Howard Hughes Medical Institute and is supported by NIH grants AI075039, AI063302 and AI155634.

Author Contributions

Conceptualization: D.I.K. and R.E.V. Investigation: D.I.K., O.V.L., and D.X.J. Data analysis: D.I.K., O.V.L., and B.A.R. Methodology: S.S. and M.M. Resources: C.G. and D.L.J. Writing: D.I.K. and R.E.V. with input from all co-authors. Funding acquisition: D.I.K. and R.E.V. Supervision: D.I.K. and R.E.V.

Declaration of Interests

R.E.V. consults for Tempest Therapeutics and X-biotix Therapeutics.

Figure Legends

Figure 1. Neutrophils and interstitial macrophages localize to diseased tissue, with macrophages localizing closer to *Mtb*. (**A**) Number of neutrophils, monocytes, IMs, and AMs in the lungs of *Mtb*-infected *Sp140*$^{-/-}$ (n = 13), *Sp140*$^{-/-}$ *Ifnar1*$^{-/-}$ (n = 11), *Acod1*$^{+/+}$ (n = 7), *Acod1*$^{+/-}$ (n = 6), *Acod1*$^{-/-}$ (n = 12), *Nos2*$^{+/+}$ (n = 4), *Nos2*$^{+/-}$ (n = 7), and *Nos2*$^{-/-}$ (n = 8) mice. (**B**) Representative images and (**C**) image quantification of *Mtb* (*Mtb*-mCherry^{+}, red), macrophages (SIRPα^{+}, blue), and neutrophils (Ly6G^{+}, green) in diseased and healthy portions of *Mtb*-infected B6 (n = 5) and *Sp140*$^{-/-}$ lungs (n = 6). (**D**) Representative images and (**E**) image quantification of *Mtb* (*Mtb*-mCherry^{+}, purple), macrophages (SIRPα^{+}, green), CD4^{+} T cells (CD4^{+}, yellow), and neutrophils (Ly6G^{+}, red) in diseased and healthy portions of *Mtb*-infected B6 (n = 6), *Acod1*$^{-/-}$ (n = 6), and *Nos2*$^{-/-}$ lungs (n = 6). (**F**) Quantification of the distance between macrophages or neutrophils to the nearest *Mtb* in representative images of B6, *Sp140*$^{-/-}$, *Acod1*$^{-/-}$, and *Nos2*$^{-/-}$ lungs. Lungs were analyzed for the experiments depicted in (A) – (F) 24-26 days after *Mtb*-Wasabi or *Mtb*-mCherry infection. The bars in (A) represent the median. Pooled data from two independent experiments are shown in (A), (C), and (E). Statistical significance in (A) by one-way ANOVA with Tukey's multiple comparison test, in (C) and (E) by paired t test, and in (F) by two tailed t test. *p < 0.05, **p < 0.01, ***p < 0.001, ****p < 0.0001.

Figure 2. *Nos2*- and *Acod1*-deficient mice mimic human *Mtb* progression but do not exhibit type I interferon-driven susceptibility. (**A**) Visualizing lung myeloid cell populations in a scRNA-seq dataset of cells from *Mtb*-infected B6, *Nos2*$^{-/-}$, *Acod1*$^{-/-}$, and *Sp140*$^{-/-}$ mice (n = 3 per genotype). (**B**) ROC curves of the ability of genes induced by *Mtb* infection in B6, *Nos2*$^{-/-}$, *Acod1*$^{-/-}$, or *Sp140*$^{-/-}$ mice to stratify human active *Mtb* patients (n = 151) and healthy controls (n = 98) in the TANDEM cohort (analysis of GSE114192) as well as stratifying human active *Mtb* patients (n = 16) and LTBI individuals (n = 31) in the Berry South Africa cohort (analysis of GSE107992). (**C**) UMAP plot and (**D**) quantification of myeloid cells undergoing type I interferon and/or IFN-γ signaling in the lungs of naïve or *Mtb*-infected B6, *Nos2*$^{-/-}$, *Acod1*$^{-/-}$, or *Sp140*$^{-/-}$ mice (n = 3 per genotype and infection status). (**E**) Lung bacterial burden in B6 (n = 10), *Sp140*$^{-/-}$ (n = 11), and *Sp140*$^{-/-}$ *Ifnar1*$^{-/-}$ (n = 12) mice infected with *Mtb*. (**F**) Lung bacterial burden in littermate control (n = 16), *Acod1*$^{-/-}$ *Ifnar1*$^{+/-}$ (n = 12), and *Acod1*$^{-/-}$ *Ifnar1*$^{-/-}$ (n = 9) mice infected with *Mtb*. (**G**) Lung bacterial burden in *Nos2*$^{+/+}$ littermate control (n = 4), *Nos2*$^{+/-}$ littermate control (n = 9), *Nos2*$^{+/-}$ *Ifnar1*$^{-/-}$ (n = 10), *Nos2*$^{-/-}$ (n = 8), and *Nos2*$^{-/-}$ *Ifnar1*$^{-/-}$ (n = 11) mice infected with *Mtb*. Lungs were analyzed 25-27 days after *Mtb*-Wasabi infection. The bars in (E), (F), and (G) represent the median. Pooled data from two independent experiments are shown in

(E), (F), and (G). Statistical significance in (D), (E), (F), and (G) by one-way ANOVA with Tukey's multiple comparison test. *p < 0.05, **p < 0.01, ***p < 0.001, ****p < 0.0001.

Figure 3. *Spp1*$^{+}$ macrophage differentiation and their expression of immunosuppressive molecules, including IL-1 receptor antagonist, correlates with *Mtb* susceptibility in mice and is conserved between mice, *Mtb*-infected non-human primates, and *Mtb*-infected humans. (**A**) Lung *Mtb*-infected monocyte and macrophage expression of *Spp1, Trem2,* and *Cxcl9*, (**B**) the resulting cell annotation, and (**C**) lung *Mtb*-infected monocyte and macrophage populations visualized separately for B6, *Nos2*$^{-/-}$, *Acod1*$^{-/-}$, and *Sp140*$^{-/-}$ mice (n = 3 per genotype). (**D**) Quantification of the frequency of *Mtb*-infected IMs, *Spp1*$^{+}$ IMs, and *Trem2*$^{+}$ IMs among all IMs for B6, *Nos2*$^{-/-}$, *Acod1*$^{-/-}$, and *Sp140*$^{-/-}$ mice (n = 3 per genotype). (**E**) Volcano plot of the differentially expressed genes in *Mtb*-infected *Spp1*$^{+}$ IMs relative to *Trem2*$^{+}$ IMs (combined analysis of cells from B6, *Nos2*$^{-/-}$, *Acod1*$^{-/-}$, and *Sp140*$^{-/-}$ mice). (**F**) *Il1rn* expression measured by scRNA-seq of *Mtb*-infected myeloid cell populations in the lungs of B6, *Nos2*$^{-/-}$, *Acod1*$^{-/-}$, and *Sp140*$^{-/-}$ mice (n = 3 per genotype). (**G**) Cell clustering and (**H**) volcano plot of the differentially expressed genes in SPP1^{+} IMs relative to TREM2^{+} IMs for cells from IgG control antibody-treated *Mtb*-infected non-human primate granulomas (analysis of https://fairdomhub.org/studies/1134). (**I**) Cell clustering and (**J**) volcano plot of differentially expressed genes in SPP1^{+} IMs relative to TREM2^{+} IMs from 18F-FDG high (n = 5) and low (n = 6) portions of lung resections from *Mtb*-infected humans (analysis of GSE192483). (**K**) *IL1RN* expression by innate immune cells in FDG high and low signal portions of *Mtb*-infected human lungs as measured by scRNA-seq (analysis of GSE192483). (**L**) ROC curve depicting the ability of *IL1RN* expression to stratify human active *Mtb* patients (n = 151) and healthy controls (n = 98) in the TANDEM cohort (analysis of GSE114192). (**M**) ROC curve depicting the ability of *IL1RN* expression to stratify human active *Mtb* patients (n = 16) and LTBI individuals (n = 31) in the Berry South Africa cohort (analysis of GSE107992). Lungs were analyzed for the experiments depicted in (A) – (F) 25 days after *Mtb*-Wasabi infection and 6 weeks after *Mtb* infection for those depicted in (G) and (H). The bars in (D) represent the median. Statistical significance in (E), (F), (H), and (J) was calculated with the Wilcoxon Rank-Sum test with Bonferroni correction and in (D) by two-way ANOVA with Tukey's multiple comparison test. ****p < 0.0001.

Figure 4. *Spp1*$^{+}$ and *Trem2*$^{+}$ macrophage differentiation is identifiable by flow cytometry and does not overlap with M1 vs M2 macrophage differentiation. (**A**) Lung *Mtb*-infected monocyte and macrophage expression of *Cd9, Cd63,* and *Itgax* plotted alongside annotated myeloid cell clusters for the *Mtb*-infected lung scRNA-seq dataset (combined analysis of cells from B6, *Nos2*$^{-/-}$, *Acod1*$^{-/-}$, and *Sp140*$^{-/-}$ mice, n = 3 per genotype). (**B**) Gating scheme used to identify mature IMs (PD-L1^{hi} CD11c^{hi}) as well as mature *Spp1*$^{+}$ IMs (PD-L1^{hi} CD11c^{hi} CD9^{hi} CD63^{low}) and mature *Trem2*$^{+}$ IMs (PD-L1^{hi} CD11c^{hi} CD9^{low} CD63^{hi}) in B6 and *Sp140*$^{-/-}$ mice. (**C**) Representative histogram depicting *Spp1*$^{+}$ IM (red), *Trem2*$^{+}$ IM (blue), and IM (grey) expression of Alcam, Trem2, and C1q in the lungs of *Mtb*-infected mice. (**D**) Quantification of the frequency of the total mature IMs, (**E**) mature *Spp1*$^{+}$ IMs, and (**F**) mature *Trem2*$^{+}$ IMs in the lungs of *Mtb*-infected B6 (n = 9), *Sp140*$^{-/-}$ (n = 16), *Nos2*$^{-/-}$ (n = 13), and *Acod1*$^{-/-}$ (n = 9) mice. (**G**) UMAP visualization comparing the frequency of the monocyte and macrophage clusters for bystander cells versus *Mtb*-infected cells (combined analysis of cells from B6, *Nos2*$^{-/-}$, *Acod1*$^{-/-}$, and *Sp140*$^{-/-}$ mice, n = 3 per genotype). (**H**) Flow cytometric analysis of *Mtb* infection frequency among IM, *Spp1*$^{+}$ IM, and *Trem2*$^{+}$ IM in the lungs of B6 (n = 13) and *Sp140*$^{-/-}$ mice (n = 12). (**I**) Frequency of iNOS^{+} and Arg1^{+} cells among IMs in *Mtb*-infected lungs from B6 (n = 9) and *Sp140*$^{-/-}$ (n = 12) mice. (**J**) scRNA-seq analysis of Nos2 and Arg1 expression in monocytes and macrophages from *Mtb*-infected lungs of B6, *Sp140*$^{-/-}$, *Nos2*$^{-/-}$, and *Acod1*$^{-/-}$ mice (n = 3 per genotype). (**K**) Representative histogram of Arg1 and iNOS expression by mature *Trem2*$^{+}$ IM

(blue), mature *Spp1*$^{+}$ IM (red), mature IM (green), and monocytes (grey) from *Mtb*-infected mouse lungs. Lungs were analyzed 24-28 days after *Mtb* or *Mtb*-Wasabi infection. The bars in (D) – (F), (H), and (I) represent the median. Pooled data from two independent experiments are shown in (D) – (F), (H), and (I). Statistical significance in (H) was calculated by one-way ANOVA with Tukey's multiple comparison test and in (D) – (F) and (I) by two-tailed t test. *p < 0.05, **p < 0.01, ***p < 0.001, ****p < 0.0001.

Figure 5. Macrophage-derived IL-1Ra is a conserved driver of *Mtb* susceptibility. (**A**) Lung bacterial burden in B6 (n = 10) and *Il1rn*$^{-/-}$ mice (n = 9) following *Mtb* infection. (**B**) Lung bacterial burden in Mrp8^{Cre-} *Il1rn*$^{fl/fl}$ (n = 5) and Mrp8^{Cre+} *Il1rn*$^{fl/fl}$ mice (n = 6) following *Mtb* infection. (**C**) Lung bacterial burden in *Sp140*$^{-/-}$ (n = 14), *Sp140*$^{-/-}$ *Il1rn* $^{+/-}$ (n = 16), *Sp140*$^{-/-}$ *Il1rn*$^{-/-}$ (n = 8), and *Sp140*$^{-/-}$ *Ifnar1*$^{-/-}$ mice (n = 15) following *Mtb* infection. (**D**) Lung bacterial burden and (**E**) neutrophil numbers in *Acod1*$^{+/-}$ *Il1rn*$^{+/+}$ (n = 7), *Acod1*$^{-/-}$ *Il1rn*$^{+/+}$ (n = 14), *Acod1*$^{-/-}$ *Il1rn*$^{+/-}$ (n = 28), and *Acod1*$^{-/-}$ *Il1rn*$^{-/-}$ (n = 8) mice following *Mtb* infection. (**F**) Lung bacterial burden in B6 (n = 7), *Acod1*$^{-/-}$ Mrp8^{Cre-} *Il1rn*$^{fl/fl}$ (n = 9) and *Acod1*$^{-/-}$ Mrp8^{Cre+} *Il1rn*$^{fl/fl}$ mice (n = 9) following *Mtb* infection. (**G**) Lung bacterial burden and (**H**) neutrophil numbers in *Nos2*-sufficient controls (n = 11), *Nos2*$^{-/-}$ *Il1rn*$^{+/+}$ (n = 8-16), *Nos2*$^{-/-}$ *Il1rn*$^{+/-}$ (n = 8-18), *Nos2*$^{-/-}$ *Il1rn*$^{-/-}$ (n = 6-19), littermate control (n = 6) and B6 (n = 5) mice following *Mtb* infection. (**I**) Lung bacterial burden in B6 (n = 9), *Nos2*$^{-/-}$ Mrp8^{Cre-} *Il1rn*$^{fl/fl}$ (n = 19) and *Nos2*$^{-/-}$ Mrp8^{Cre+} *Il1rn*$^{fl/fl}$ mice (n = 11) following *Mtb* infection. (**J**) Lung *Mtb* burden in *Sp140*$^{+/-}$ littermate control (n = 19), *Sp140*$^{-/-}$ littermate control (n = 19), and *Sp140*$^{-/-}$ *Il1rn*$^{fl/fl}$ *CD64*$^{cre+}$ (n = 24) mice. Lungs were analyzed 24-28 days after *Mtb* or *Mtb*-Wasabi infection. The bars in (A) – (J) represent the median. Pooled data from two independent experiments are shown in (A) – (I) and three independent experiments in (J). Statistical significance in (A) and (B) was calculated with a two-tailed t test while in (C) - (J) it was calculated by one-way ANOVA with Tukey's multiple comparison test. *p < 0.05, **p < 0.01, ***p < 0.001, ****p < 0.0001.

Figure 6. IL-1 enhances cytokine and chemokine expression by Th17, NKT17, and ILC3 as well as stromal cells. (**A**) Schematic of the BM chimera mice used in panels (B) – (G). (**B**) T cell populations and (**C**) their expression of *Il1r1* in the *Mtb*-infected lungs of the BM chimera mice. (**D**) Volcano plot of the differentially expressed genes in the WT Th17 cells relative to *Il1r1*$^{-/-}$ Th17 cells during *Mtb* infection. (**E**) Innate lymphoid cell populations and (**F**) their expression of *Il1r1* in the *Mtb*-infected lungs of the BM chimera mice. (**G**) Differentially expressed genes in the WT ILC3 and NKT17 cells relative to *Il1r1*$^{-/-}$ cells during *Mtb* infection. (**H**) Schematic of the BM chimera mice used in panels (I) – (K). (**I**) Non-hematopoietic cell populations and (**J**) their expression of *Il1r1* in the *Mtb*-infected lungs of the BM chimera mice. (**K**) Differentially expressed genes in the WT myofibroblast, fibroblast, and endothelial cells relative to *Il1r1*$^{-/-}$ cells during *Mtb* infection. (**I**) Schematic of the BM chimera mice used in panel (M). (**M**) Lung *Mtb* burden in BM chimera mice that received *Il1r1*$^{-/-}$: CD45.1 mixed BM (n = 8), *Il1r1*$^{-/-}$: *Il17*$^{-/-}$ *Il22*$^{-/-}$ mixed BM (n = 10), or *Il1r1*$^{-/-}$ BM (n = 13). Lungs were analyzed 25 days after *Mtb*-Wasabi infection. The bars in (M) represent the median. Pooled data from two independent experiments are shown in (M). Statistical significance in (D), (G), and (K) was calculated with the Wilcoxon Rank-Sum test with Bonferroni correction and in (M) by one-way ANOVA with Tukey's multiple comparison test. *p < 0.05.

Materials and Methods

Mice. Following University of California Berkeley Institutional Animal Care and Use Committee regulatory standards, mice were housed at 23°C with a 12-hour light-dark cycle and maintained under specific pathogen-free conditions. Male and female mice were used for experiments. Mice

were age-matched with littermate controls when possible and 6-12 weeks old at the start of the infections. C57BL/6 (B6), B6.129S2-Ifnar1^{tm1Agt}/Mmjax (*Ifnar1*$^{-/-}$)[123], B6.SJL-*Ptprc*^{a} *Pepc*^{b}/BoyJ (CD45.1)[124], B6.129S7-*Il1r1*^{tm1Imx}/J (*Il1r1*$^{-/-}$)[125], B6.129(Cg)-*Il1r1*$^{tm1.1Rbl}$/J (*Il1r1*$^{fl/fl}$)[126], B6.129P2-*Avil*$^{tm2(cre)Fawa}$/J (Adv^{Cre})[127], B6.129P2-*Nos2*^{tm1Lau}/J (*Nos2*$^{-/-}$)[128], and C57BL/6NJ-*Acod1*$^{em1(IMPC)J}$/J (*Acod1*$^{-/-}$) mice were purchased from Jackson Laboratories. B6-Fcgr1^{tm2Ciphe} (CD64^{Cre})[67] mice were a gift from B. Malissen at Centre d'Immunologie de Marseille Luminy and were provided by Y. Belkaid at the National Institutes of Health. BM from *Il17*$^{-/-}$*Il22*$^{-/-}$ mice was a gift from S. Khader at the University of Chicago. Il1rn$^{tm1.1Cga}$ *(Il1rn*^{fl})[68] were generated by Cem Gabay at the University of Geneva and were provided by A. Luster at Massachusetts General Hospital. *Sp140*$^{-/-}$ mice were previously generated in-house[14]. *Sp140*$^{-/-}$ *Ifnar1*$^{-/-}$, *Acod1*$^{-/-}$ *Ifnar1*$^{-/-}$, and *Nos2*$^{-/-}$ *Ifnar1*$^{-/-}$ mice were generated by crossing *Sp140*$^{-/-}$, *Acod1*$^{-/-}$, and *Nos2*$^{-/-}$ mice with *Ifnar1*$^{-/-}$ mice in-house, respectively. *Sp140*$^{-/-}$, *Acod1*$^{-/-}$, and *Nos2*$^{-/-}$ mice were crossed in-house with *Il1rn*$^{-/-}$ mice to generate *Sp140*$^{-/-}$ *Il1rn*$^{-/-}$, *Acod1*$^{-/-}$ *Il1rn*$^{-/-}$, and *Nos2*$^{-/-}$ *Il1rn*$^{-/-}$ mice. *Sp140*$^{-/-}$ *Il1rn*$^{fl/fl}$ CD64^{Cre} mice were generated by crossing *Sp140*$^{-/-}$ mice with *Il1rn*$^{fl/fl}$ and CD64^{Cre} mice in-house. *Acod1*$^{-/-}$ *Il1rn*$^{fl/fl}$ Mrp8^{Cre} mice and *Nos2*$^{-/-}$ *Il1rn*$^{fl/fl}$ Mrp8^{Cre} mice were generated by crossing *Acod1*$^{-/-}$ or *Nos2*$^{-/-}$ mice with *Il1rn*$^{fl/fl}$ and Mrp8^{Cre} mice in-house. Adv^{Cre} *Il1r1*$^{fl/fl}$ and CD64^{Cre} *Il1r1*$^{fl/fl}$ mice were generated by crossing Adv^{Cre} and CD64^{Cre} mice with *Il1r1*$^{fl/fl}$ mice in-house.

Bone marrow chimera mice. Adult mice were lethally irradiated with a Precision X-Rad320 X-Ray irradiator (North Branford, CT) using a split dose of 500 rads each round with irradiation occurring 4-12 hours apart. Bone marrow (BM) from donor mice indicated in the figures was prepared by mashing femurs with a mortar and pestle to generate a single cell suspension. Red blood cells were then lysed with ACK lysis buffer (Thermo Fisher Scientific). The cells were then diluted in PBS and 1 × 10^7 cells (either all one genotype or a 1 : 1 mix of two genotypes for mixed BM chimera mice) were retro-orbitally injected into each recipient mouse. Mice were housed for at least 8 weeks post-injection to permit hematopoietic reconstitution prior to their use in experiments.

***Mtb* infections**. *Mtb* expressing Wasabi (*Mtb*-Wasabi) and *Mtb*-mCherry were generated using *Mtb* Erdman, a gift from S. A. Stanley, that had been passaged 2 or fewer times *in vitro*. *Mtb* was transformed with the pTEC15 plasmid (a gift from Lalita Ramakrishnan; Addgene plasmid # 30174)[129] or the pMSP12::mCherry plasmid (a gift from Lalita Ramakrishnan; Addgene plasmid # 30167) to generate *Mtb*-Wasabi and *Mtb*-mCherry, respectively. For the transformation, *Mtb* was cultured in Middlebrook 7H9 liquid medium supplemented with 10% albumin-dextrose-saline, 0.4% glycerol, and 0.05% Tween-80 for 5 days at 37°C then washed in 10% glycerol to remove salts. Washed *Mtb* was electroporated with 1 µg DNA using a 2 mm electroporation cuvette and the following settings: 2500 volts, 1000 Ohms, 25 µF. Electroporated *Mtb* was grown on 7H11 plates supplemented with 10% oleic acid, albumin, dextrose, and catalase, 0.5% glycerol, and either 200 µg / mL Hygromycin for *Mtb*-Wasabi or 50 µg / mL Kanamycin for *Mtb*-mCherry for 3-4 weeks at 37°C. Colonies were picked and cultured in 10 mL inkwell flasks for 7 days at 37°C and then expanded into a 100 mL culture for 4-5 days at 37°C using 7H9 medium supplemented with 10% albumin-dextrose-saline, 0.4% glycerol, 0.05% Tween-80, and either Hygromycin for *Mtb*-Wasabi or Kanamycin for *Mtb*-mCherry. At log phase, the Mtb was filtered through a 5 µm syringe filter and frozen in 1 mL aliquots in 10% glycerol. Frozen cultures were diluted in distilled water to an O.D. of 0.0017 and then aerosolized with an inhalation exposure system (Glas-Col, Terre Haute, IN) thereby delivering ~10-100 *Mtb* per mouse as determined by plating lungs day 1 post-infection to assess bacterial burden.

Tissue Processing for CFU and Flow cytometry. Mice were harvested at 24-28 days following *Mtb* infection. Lungs were collected in gentleMACS C tube (Miltenyi Biotec) containing

3 mL of RPMI media with 70 µg / mL of Liberase TM (Roche) and 30 µg / mL of DNase I (Roche) and then processed into chunks using the lung_01 setting on a gentleMACS (Miltenyi Biotec). Samples were then digested at 37°C for 30 minutes before being homogenized with the lung_02 setting on the gentleMACS. 2 mL of PBS with 20% Newborn Calf Serum (Thermo Fisher Scientific) were added to each sample to quench the digest before samples were filtered through 70 µm SmartStrainers (Miltenyi Biotec).

Measuring Bacterial Burden. *Mtb* burden was assessed by serial dilution of the lung single cell suspension in phosphate-buffered saline (PBS) with 0.05% Tween-80. The dilutions were plated on 7H11 plates supplemented with 10% oleic acid, albumin, dextrose, and catalase and 0.5% glycerol and colonies were counted ~3 weeks after plating.

Flow Cytometry. Flow cytometry was performed by staining 100 µLs of lung single cell suspension with antibodies in PBS with 2% Newborn Calf Serum and 0.05% Sodium azide. A fixable viability dye (Ghost Dye Violet 510 or 540 or Red 780; Tonbo Biosciences), Super Bright Complete Staining Buffer (Thermo Fisher Scientific), and True-Stain Monocyte Blocker (BioLegend) were also added to every sample during surface antibody staining. Surface stains were incubated for 30-60 minutes at room temperature using a selection of the following antibodies: TruStain FcX PLUS (S17011E, BioLegend), BUV496-labeled CD45 (30-F11, BD Biosciences), BUV395-labeled CD11b (M1/70, BD Biosciences), BUV737-labeled CD11c (HL3, BD Biosciences), APC-R700-labeled Siglec F (E50-2440, BD Biosciences), PE-labeled MerTK (DS5MMER, Thermo Fisher Scientific), Super Bright 645-labeled MHC II (M5/114.15.2, Thermo Fisher Scientific), BV421-labeled PD-L1 (MIH5, BD Biosciences), BV711-labeled Ly6C (HK1.4 , BioLegend), PE-Cy7-labeled MerTK (DS5MMER, Thermo Fisher Scientific), APC-labeled CD64 (X54-5/7.1, BioLegend), BUV563-labeled Ly6G (1A8, BD Biosciences), BV605-labeled MHC II (M5/114.15.2, BioLegend), Percp-Cy5.5-labeled CD9 (MZ3, BioLegend), eFluor 450-labeled Ly6D (49-H4, Thermo Fisher Scientific), BV480-labeled Fcer1a (MAR-1, BD Biosciences), BV650-labeled CD8α (53-6.7, BioLegend), BV785-labeled CD16.2 (9E9, BioLegend), AF594-labeled TREM2 (237920, R&D systems), AF647-labeled XCR1 (ZET, XCR1), APC-Fire 750-labeled CD19 (6D5, BioLegend), APC-Fire 750-labeled CD90.2 (30-H12, BioLegend), BUV615-labeled SIRPα (P84, BD Biosciences), BUV661-labeled B220 (RA3-6B2, BD Biosciences), PE-labeled Alcam (eBioALC48, Thermo Fisher Scientific), RB744-labeled CD9 (KMC8, BD Biosciences), BUV805-labeled PD-L1 (MIH5, BD Biosciences), and BUV805-labeled CD26 (H194-112, BD Biosciences). Following surface staining, samples were washed with PBS with 2% Newborn Calf Serum and 0.05% Sodium azide and then fixed for 20 minutes at room temperature with cytofix/cytoperm (BD biosciences) prior to removal from the BSL3. If intracellular staining was performed, samples were incubated overnight at 4°C with combinations of the following antibodies: PE-Cy7-labeled CD63 (NVG-2, BioLegend), FITC-labeled C1q (JL-1, Thermo Fisher Scientific), AF700-labeled CD63 (NVG-2, BioLegend), eFluor 450-labeled Arg1 (A1exF5, Thermo Fisher Scientific), AF532-labeled iNOS (CXNFT, Thermo Fisher Scientific), and Percp-eFluor 710-labeled iNOS (CXNFT, Thermo Fisher Scientific). After washing out the intracellular stain, each sample received AccuCheck Counting Beads (Invitrogen) and was then analyzed on an Aurora (Cytek) flow cytometer. Data were analyzed with Flowjo version 10 (BD Biosciences).

Confocal microscopy. A Zeiss LSM 880 laser scanning confocal microscope with 405, 458, 488, 514, 561, 594, and 633 lasers, with two photomultiplier detectors, a 34-channel GaASP spectral detector system, and a 2-channel AiryScan detector was used for microscopy. 20 µm sections were prepared from paraformaldehyde-fixed lungs from *Mtb*-mCherry-infected B6 and *Sp140*$^{-/-}$ mice. The sections were stained overnight at 4°C with the following antibodies: BV421-labeled SIRPα (P84, BD Biosciences), Pacific Blue–labeled B220 (RA3-6B2, BioLegend),

eF506-labeled CD4 (RM4-5, BioLegend), and AF647-labeled Ly6G (1A8, BioLegend). Diseased and healthy lesions were identified in stained sections with a 5× air objective and then imaged as a 20 µm z-stack acquired at a 1.5 µm step size with a 63× oil immersion objective lens with a numerical aperture of 1.4. The 63× oil immersion objective lens with a numerical aperture of 1.4 was also used to image single color-stained Ultracomp eBeads Plus (Thermo Fisher Scientific) for generating a compensation matrix.

Image processing and histo-cytometry analysis. The Generate Compensations Matrix script[130] was used in ImageJ to create a compensation matrix based on the single color-stained control images of the Ultracomp eBeads Plus (Thermo Fisher Scientific). The resulting compensation matrix was used for spectral unmixing of the lung images using Chrysalis software[130], which was also used to rescale the data and generate new channels based on mathematical operations performed on existing channels. Imaris 9.9.1 (Bitplane) was used on the processed lung images to digitally identify cells based on protein expression using the surface creation tool and to measure the distance between *Mtb* and the nearest macrophage or neutrophil[131]. Statistics for the identified cells were exported from Imaris and then imported into FlowJo version 10 (BD Biosciences) for quantitative image analysis.

Sorting Immune Cells for scRNA-seq analysis. For the myeloid dataset, lungs from 3 *Mtb*-Wasabi-infected as well as from 3 naïve *Acod1*$^{-/-}$ and 3 naïve *Nos2*$^{-/-}$ mice were processed as described for CFU and flow cytometry analysis 25 days after infection with the following slight modification: 3 minutes before harvesting, 0.25 µg of TotalSeq-A-labeled CD45.2 (104, BioLegend) was intravenously injected into each mouse to label cells in the vasculature[132]. Surface staining of lung single cell suspensions was performed in PBS with 2% Newborn Calf Serum on ice for 30 minutes with the following antibodies: TruStain FcX PLUS (S17011E, BioLegend), APC-labeled Ly6G (1A8, BioLegend), APC-labeled CD64 (X54-5/7.1, BioLegend), and TotalSeq-A-labeled Ly6G (1A8, BioLegend). Magnetic enrichment was then performed with the EasySep APC Positive Selection Kit II (StemCell Technologies) and MojoSort Magnets (BioLegend) to increase the frequency of myeloid cells within the sample prior to sorting. Following enrichment, samples were stained on ice for 45 minutes in PBS with 2% Newborn Calf Serum and True-Stain Monocyte Blocker (BioLegend) using a combination of the following antibodies: TotalSeq-A-labeled Ly6C (HK1.4, BioLegend), TotalSeq-A-labeled CD44 (IM7, BioLegend), TotalSeq-A-labeled CD274 (MIH6 , BioLegend), TotalSeq-A-labeled Siglec F (S17007L, BioLegend), TotalSeq-A-labeled CSF1R (AFS98, BioLegend), TotalSeq-A-labeled CD11b (M1/70, BioLegend), TotalSeq-A-labeled CD86 (GL-1, BioLegend), TotalSeq-A-labeled MHC II (M5/114.15.2, BioLegend), TotalSeq-A-labeled CX3CR1 (SA011F11, BioLegend), TotalSeq-A-labeled CD11c (N418, BioLegend), TotalSeq-A-labeled CCR2 (SA203G11, BioLegend), TotalSeq-A-labeled CD62L (MEL-14, BioLegend), anti-mouse TotalSeq-A Hashtag antibody (1-6; BioLegend), PE-labeled Siglec F (S17007L, BioLegend), Pacific Blue-labeled B220 (RA3-6B2, BioLegend), and Pacific Blue-labeled CD90.2 (53-2.1, BioLegend). The TotalSeq-A-labeled antibodies detect protein expression in the scRNA-seq dataset, while the Hashtag antibodies allow several samples to be multiplexed together in a single lane on a 10X Genomics Chromium Next GEM Chip[133]. After staining, the samples were incubated with Sytox Blue Dead Cell Stain (Thermo Fisher Scientific) and sort purified using a 100 µm sorting chip in a 4 laser SH-800 cell sorter (Sony) on the purity setting. For *Mtb*-infected mice, *Mtb*-infected cells and bystander myeloid cells were individually purified, while samples from naïve lungs were sorted as macrophages and a mixture of neutrophils and monocytes that were then combined at a 1:2 ratio for greater representation of macrophages in the scRNA-seq dataset.

The stromal cell dataset was generated by infecting BM chimera mice made by transferring CD45.1 BM into lethally irradiated B6 or *Il1r1*$^{-/-}$ hosts with *Mtb* 8 weeks post-reconstitution. Lungs from the infected animals as well as naïve chimera mice were harvested

and processed as described for CFU and flow cytometry analysis. ACK lysing buffer (Thermo Fisher Scientific) was used to lyse the red blood cells in the samples, which were then stained for 30 minutes on ice with TruStain FcX PLUS (S17011E, BioLegend) and PE-Cy7-labeled CD45 (30-F11, BioLegend) antibody. The EasySep PE Positive Selection Kit II (StemCell Technologies) and MojoSort Magnets (BioLegend) were used to perform negative selection to enrich the $CD45^-$ non-hematopoietic cells. The enriched cells were incubated with Sytox Green Dead Cell Stain (Thermo Fisher Scientific) and live $CD45^-$ were sort purified using a 130 µm sorting chip in a 4 laser SH-800 cell sorter (Sony) on the purity setting.

The T cell and ILC datasets were generated by *Mtb* infection of mixed BM chimera mice generated by transferring WT CD45.1/2 and *Il1r1*$^{-/-}$ BM into lethally irradiated CD45.1 mice. Lungs were harvested 25 days post-infection and processed as described for measuring CFU and performing flow cytometry. Three mice were used for the T cell dataset, while the rarity of the ILCs required pooling lungs into 3 samples (2 samples containing 5 lungs and 1 sample containing 6 lungs). The T cell samples were treated with ACK lysing buffer (Thermo Fisher Scientific) to lyse the red blood cells and then stained on ice for 30 minutes with the following antibodies: BV421-labeled CD45.1 (A20, BioLegend), BV785-labeled CD45.2 (104, BioLegend), PE-labeled CD3e (17A2, BioLegend), APC-labeled CD11b (M1/70, Cytek), APC-labeled CD11c (N418, Cytek), APC-labeled CD19 (1D3, Cytek), TotalSeq-A-labeled Ly6C (HK1.4, BioLegend), TotalSeq-A-labeled CD44 (IM7, BioLegend), TotalSeq-A-labeled CD274 (MIH6 , BioLegend), TotalSeq-A-labeled CX3CR1 (SA011F11, BioLegend), TotalSeq-A-labeled CD62L (MEL-14, BioLegend), TotalSeq-A-labeled TCRβ (H57-597, BioLegend), TotalSeq-A-labeled CD49a (, BioLegend), TotalSeq-A-labeled CD49a (HMα1, BioLegend), TotalSeq-A-labeled NKp46 (29A1.4, BioLegend), TotalSeq-A-labeled CD4 (RM4-5, BioLegend), TotalSeq-A-labeled ST2 (DIH9, BioLegend), TotalSeq-A-labeled CD25 (PC61, BioLegend), TotalSeq-A-labeled CD45.1 (A20, BioLegend), TotalSeq-A-labeled CD45.2 (104, BioLegend), TotalSeq-A-labeled CD8a (53-6.7, BioLegend), TotalSeq-A-labeled CXCR5 (L138D7, BioLegend), TotalSeq-A-labeled CCR6 (29-2L17, BioLegend), and anti-mouse TotalSeq-A Hashtag antibody (1-3; BioLegend). The stained T cell samples were then incubated with Sytox Green Dead Cell Stain (Thermo Fisher Scientific) and T cells (Live $CD3e^+$ $CD11b^-$ $CD11c^-$ $CD19^-$ $CD45.1^+$ or $CD45.2^+$ cells) were sort purified using a 100 µm sorting chip in a 4 laser SH-800 cell sorter (Sony) on the purity setting.

The ILC samples treated with ACK lysing buffer (Thermo Fisher Scientific) were stained on ice for 25 minutes with the following panel of lineage-specific antibodies: Biotin-labeled TER-119 (TER-119, BioLegend), Biotin-labeled GR-1 (RB6-8C5, BioLegend), Biotin-labeled CD3e (145-2C11, BioLegend), Biotin-labeled CD11b (M1/70, BioLegend), Biotin-labeled B220 (RA3-6B2, BioLegend), and Biotin-labeled TCRγ/δ (GL3, BioLegend). $Lineage^-$ cells were enriched by negative selection using the EasySep Streptavidin RapidSpheres Isolation Kit (StemCell Technologies) and MojoSort Magnets (BioLegend). Enriched samples were then stained on ice for 30 minutes with the following antibodies: BV421-labeled CD45.1 (A20, BioLegend), BV785-labeled CD45.2 (104, BioLegend), PE-labeled CD127 (A7R34, BioLegend), Alexa Fluor 700-labeled CD127 (30-H12, BioLegend), Biotin-labeled CD5 (53-7.3, BioLegend), Biotin-labeled TCRβ (H57-597, BioLegend), TotalSeq-A-labeled Ly6C (HK1.4, BioLegend), TotalSeq-A-labeled CD44 (IM7, BioLegend), TotalSeq-A-labeled CD274 (MIH6 , BioLegend), TotalSeq-A-labeled CX3CR1 (SA011F11, BioLegend), TotalSeq-A-labeled CD62L (MEL-14, BioLegend), TotalSeq-A-labeled TCRβ (H57-597, BioLegend), TotalSeq-A-labeled CD49a (, BioLegend), TotalSeq-A-labeled CD49a (HMα1, BioLegend), TotalSeq-A-labeled NKp46 (29A1.4, BioLegend), TotalSeq-A-labeled CD4 (RM4-5, BioLegend), TotalSeq-A-labeled ST2 (DIH9, BioLegend), TotalSeq-A-labeled CD25 (PC61, BioLegend), TotalSeq-A-labeled CD45.1 (A20, BioLegend), TotalSeq-A-labeled CD45.2 (104, BioLegend), TotalSeq-A-labeled CD8a (53-6.7, BioLegend), TotalSeq-A-labeled CXCR5 (L138D7, BioLegend), TotalSeq-A-labeled CCR6 (29-2L17, BioLegend), and anti-mouse TotalSeq-A Hashtag antibody (4-6; BioLegend). The enriched samples were then stained with APC-labeled Streptavidin (BioLegend) for 15 minutes

on ice before being stained with Sytox Green Dead Cell Stain (Thermo Fisher Scientific). ILCs (Lineage$^-$ IL-7Ra$^+$ CD90.2$^+$ CD45.1$^+$ or CD45.2$^+$ cells) were sort purified using a 100 µm sorting chip in a 4 laser SH-800 cell sorter (Sony) on the purity setting.

Single cell RNA: Library generation and sequencing. The v3.1 chemistry Chromium Single Cell 3' Reagent Kit (10X Genomics) was used to generate scRNA-seq libraries using the CITE-seq protocol[48] modifications for the myeloid, T, and innate lymphoid cell libraries and the standard 10X protocol for the stromal cell library. The myeloid cell dataset required three lanes of a Chromium Next GEM Chip, with lane 1 containing naïve cells, lane 2 containing *Mtb*-infected cells, and lane 3 containing the bystander cells from the 3 *Acod1*$^{-/-}$ and 3 *Nos2*$^{-/-}$ mice. Each lane was super-loaded with ~34,000 cells for a target of 17,000 single cells per lane at a multiplet rate of 3%[133]. The stromal cell dataset used 4 lanes of a Chromium Next GEM Chip, with lane 1 containing *Il1r1*$^{-/-}$ stromal cells from *Mtb*-infected mice, lane 2 containing *Il1r1*$^{-/-}$ stromal cells from naïve mice, lane 3 containing wild-type stromal cells from *Mtb*-infected mice, and lane 4 containing wild-type stromal cells from naïve mice. Each lane was loaded with 12,500 cells for an expected yield of 7,000 single cells at a multiplet rate of 5%. The T cell and ILC libraries were generated using the same Chromium Next GEM Chip, with lane 1 containing T cells and lane 2 containing ILCs from *Mtb*-infected mixed BM chimera mice. 25,000 cells were super-loaded into each lane with a target capture of 13,200 cells at a multiplet rate of 4%[133]. For the CITE-seq libraries, 0.5 U/µL RNaseOUT Recombinant Ribonuclease Inhibitor (Invitrogen) was added to single cell RT master mix during the loading step and 1 µL of ADT and HTO additive primers (0.2 µM stock) were added during the cDNA amplification. All samples were decontaminated by 2 rounds of centrifugation through 0.2 µM filter microcentrifuge tubes following cDNA, ADT, and HTO purification and then removed from the BSL3. The CITE-seq protocol was used to complete the ADT and HTO libraries while the 10X Genomics protocol was followed for the cDNA library. Quality control of the libraries was performed with a Fragment Analyzer (Agilent). Libraries were pooled and then sequenced on a NovaSeq 6000 (Illumina) using an S1 flow cell and the following cycles read 1 (28 cycles), i7 index (10 cycles), i5 index (10 cycles), read 2 (90 cycles).

ScRNA-seq: data processing. Sequencing reads of the mRNA libraries were mapped to the mouse genome with CellRanger version 6.0.0 (10X Genomics), while the raw count matrices for the ADT and HTO libraries were generated with CITE-Seq-Count version 1.4.3[134]. The count matrices were analyzed with Seurat v4.3.0[47] using default settings for normalizing the data, finding variable features, and scaling the data. For CITE-seq datasets, multiplets were excluded through HTO demultiplexing using the HTODemux function. The myeloid cell dataset was filtered to include cells with between 200 and 4500 genes and less than 5% mitochondrial reads. The T cell, ILC, and stromal cell datasets were filtered to only include cells that have between 200 and 2500 genes and less than 5% mitochondrial reads. The resulting myeloid dataset as well as our previously published scRNA-seq datasets for myeloid cells in *Mtb*-infected and naïve B6 and *Sp140*$^{-/-}$ mice (GSE216023) were integrated together and then clustered with a resolution of 1.5. The T cell and ILC datasets were analyzed with the default Seurat workflow using weighted nearest neighbor multimodal analysis to cluster cells based on mRNA and protein expression at a resolution of 1. The stromal cell dataset was also analyzed with Seurat using integration to combine the *Mtb*-infected and naïve WT and *Il1r1*$^{-/-}$ datasets and then clustering the cells based on mRNA expression using a resolution of 1.5.

Bulk RNA-seq, Gene signature and ROC curve analysis. Our previously published signatures for type I IFN and IFN-γ[15] were applied to our myeloid cell scRNA-seq dataset to score cells based on their gene expression using the UCell package[135]. Signatures for the B6, *Nos2*$^{-/-}$, *Acod1*$^{-/-}$, and *Sp140*$^{-/-}$ mice were generated in R[136] by identifying genes induced at

least 8-fold in the myeloid cells from *Mtb*-infected mice relative to naïve animals for each genotype. A corresponding human signature was produced using the convert_mouse_to_human_symbols from the NichetNetr package[72]. The hacksig package using the singscore statistical method[137] was applied to calculate a signature score based on each signature's expression in the TANDEM cohort PBMC RNA-seq data[49], Berry South Africa RNA-seq data[50], or the Bloom et al. microarray data[51]. The pROC package[138] was used to generate the ROC curves and calculate the area under the curve to quantify the ability of each signature to discriminate between the active *Mtb* cases and healthy controls in the TANDEM cohort, between active *Mtb* cases and LTBI individuals in the Berry South Africa dataset, and between active *Mtb* cases and lung cancer or pneumonia in the Bloom et al. dataset. The hacksig and pROC packages were also used to test the predictive ability of a gene signature consisting of known immunosuppressive genes (*IL1RN*, *IL18BP*, *CD274*, *TGFB1*, *IDO1*, *IL10*, and *ARG1*) on the TANDEM cohort. The pROC package was also used to determine the ability of *IL1RN* expression to identify active *Mtb* cases in the TANDEM cohort and the Berry South Africa dataset. The DESeq2 package[139] was used to analyze *IL1RN* expression in human PBMCs from *Mtb*-infected or healthy control individuals in the TANDEM cohort as well as to analyze *IL1RN* expression relative to time prior to TB diagnosis in the progressor portion of the Adolescent Cohort Study[63].

NicheNet analysis of IL-1-regulated signaling. IL-1-regulated genes were defined as genes expressed at least 2-fold higher in WT than *Il1r1*$^{-/-}$ cells in the T cell, innate lymphoid cell, and stromal cell scRNA-seq datasets. These IL-1-regulated genes were used as the potential ligands for NicheNet analysis[72]. The receiver cells were defined as IMs, *Trem2*$^{+}$ IMs, and *Spp1*$^{+}$ IMs from the myeloid cell scRNA-seq dataset. The expressed receptors on the receiver cells were identified using the get_expressed_genes function from NicheNet with a 10% cutoff for expression and then filtering the NicheNet receptor database to those genes expressed in the IM populations. Ligand activity in the receiver cells was calculated by identifying genes upregulated in *Trem2*$^{+}$ or *Spp1*$^{+}$ IMs relative to the IM cell population via the FindMarkers function from the Seurat package[47], focusing on genes upregulated at least 2-fold and with an adjusted p value less than 0.05, as calculated by the Wilcoxon Rank-Sum test with Bonferroni correction. The ability of each IL-1-regulated ligand to induce the genes upregulated in *Trem2*$^{+}$ or *Spp1*$^{+}$ IMs was determined by NicheNet's predict_ligand_activities function.

Statistical analysis. Statistical significance was determined using Prism (GraphPad) software for unpaired or paired two-tailed Student t test when comparing two populations, or one-way ANOVA tests with Tukey's multiple comparisons test when comparing multiple groups. ROC curves and their AUC were calculated in R using the pROC package.

Data availability. Raw and processed single cell RNA-sequencing data is deposited at NCBI Gene Expression Omnibus: GSE255213, GSE254983, and GSE254926.

Code availability. Code for scRNA-sequencing analysis is available on Github: https://github.com/dmitrikotov/IL-1Ra-TB.

Supplementary Figure Legends

Supplementary Figure 1. Classifying myeloid scRNA-seq clusters and comparing myeloid cells from naïve *Sp140*-, *Nos2*-, and *Acod1*-deficient mouse lungs. Dot plot of lineage of markers used to (**A**) identify myeloid cell clusters and (**B**) define neutrophil cluster heterogeneity. (**C**) The myeloid populations in the naïve lungs of B6, *Nos2*$^{-/-}$, *Acod1*$^{-/-}$, and

Sp140$^{-/-}$ mice (n = 3 per genotype). (**D**) Number of shared and unique genes differentially expressed (2-fold change and adjusted p value < 0.05) between by neutrophils, alveolar macrophages, monocytes, and interstitial macrophages in *Nos2*$^{-/-}$, *Acod1*$^{-/-}$, and *Sp140*$^{-/-}$ relative to those from B6 mice. Statistical significance in (D) was calculated with the Wilcoxon Rank-Sum test with Bonferroni correction.

Supplementary Figure 2. Mouse gene signatures consisting of genes upregulated in myeloid cells following *Mtb* infection of B6, *Sp140*$^{-/-}$, *Acod1*$^{-/-}$, or *Nos2*$^{-/-}$ mice discriminate active *Mtb* infection from Cancer and Pneumonia in humans. (**A**) A heatmap depicting the $\log_2$ fold change of gene upregulation following *Mtb* infection relative to the gene's expression in myeloid cells from naïve lungs. The heatmap compares gene expression for signature genes between B6, *Nos2*$^{-/-}$, *Acod1*$^{-/-}$, and *Sp140*$^{-/-}$ mice (n = 3 per genotype). Grey boxes indicate genes not present in the gene signature of a given mouse genotype. Genes in blue indicate those with known immunosuppressive function. (**B**) ROC curves of the ability of genes induced by *Mtb* infection in B6, *Nos2*$^{-/-}$, *Acod1*$^{-/-}$, or *Sp140*$^{-/-}$ mice to stratify human active *Mtb* patients (n = 35) and individuals with lung cancer (n = 16) or Pneumonia (n = 19) in the Bloom et al. cohort (analysis of GSE42834).

Supplementary Figure 3. Classifying scRNA-seq clusters for *Mtb*-infected non-human primate and human lung datasets. Dot plot of lineage of markers used to identify cell clusters in (**A**) *Mtb*-infected non-human primate and (**B**) human lungs.

Supplementary Figure 4. Conservation of genes preferentially expressed by *Spp1*$^{+}$ IMs relative to *Trem2*$^{+}$ IMs in *Mtb*-infected susceptible mice and humans. (**A**) Venn diagram depicting the number of genes preferentially expressed (2-fold change and adjusted p value < 0.05) by *Spp1*$^{+}$ IMs relative to *Trem2*$^{+}$ IMs in *Mtb*-infected B6, *Nos2*$^{-/-}$, *Acod1*$^{-/-}$, and *Sp140*$^{-/-}$ mouse lungs (n = 3 per genotype) and human lungs (analysis of GSE192483). (**B**) Core gene signature for genes commonly expressed by *Spp1*$^{+}$ IMs in all three susceptible mouse models as well as those expressed by the three susceptible mouse models and humans.

Supplementary Figure 5. IL-1Ra expression in mice and humans. (**A**) Myeloid cell expression of *Il1r2* and *Il1rn* in naïve and *Mtb*-infected lungs from B6, *Nos2*$^{-/-}$, *Acod1*$^{-/-}$, and *Sp140*$^{-/-}$ mice (n = 3 mice per genotype for naïve lungs and 3 mice per genotype for *Mtb*-infected lungs) as measured by scRNA-seq. (**B**) *Il1rn* expression in myeloid cells from the lungs of B6, *Nos2*$^{-/-}$, *Acod1*$^{-/-}$, and *Sp140*$^{-/-}$ mice (n = 3 mice per genotype for naïve lungs and 3 mice per genotype for *Mtb*-infected lungs). (**C**) Normalized *IL1RN* expression in *Mtb*-infected (n = 151) and healthy individuals (n = 98) from the TANDEM cohort (analysis of GSE114192). (**D**) ROC curve of the predictive ability of an immunosuppressive gene signature applied to the TANDEM cohort. (**E**) *IL1RN* expression plotted relative to time before clinical diagnosis of *Mtb* infection in the progressor population of the Adolescent Cohort Study (n = 74) with the blue line indicating local polynomial regression fitting using the loess method and grey indicating the confidence interval. Day 200 prior to diagnosis (red line) indicates the timepoint *IL1RN* expression started to increase in patients as they approached diagnosis (analysis of GSE79362). Statistical significance in (C) was calculated using the Wald test and corrected for multiple testing using the Benjamini and Hochberg method.

Supplementary Figure 6. Flow cytometric identification of monocyte and monocyte-derived macrophage subsets identified by scRNA-seq. (**A**) Overview of monocyte and interstitial macrophage subsets and (**B**) their expression of subset identifying markers as measured by scRNA-seq of *Mtb*-infected lungs from B6, *Nos2*$^{-/-}$, *Acod1*$^{-/-}$, and *Sp140*$^{-/-}$ mice (n

= 3 mice per genotype). (**C**) Myeloid cell flow cytometry gating strategy. (**D**) Frequency of *Mtb*-infected cells among the major myeloid cell populations.

Supplementary Figure 7. Myeloid cells express very little IL-1 receptor and IM as well as neuronal expression of IL-1 receptor does not impact bacterial control in a cell-intrinsic manner. (**A**) The myeloid populations identified by scRNA-seq and (**B**) *Il1r1* expression in myeloid cells from the lungs of B6, *Nos2*$^{-/-}$, *Acod1*$^{-/-}$, and *Sp140*$^{-/-}$ mice (n = 3 mice per genotype for naïve lungs and 3 mice per genotype for *Mtb*-infected lungs). (**C**) Mixed BM chimera schematic, (**D**) representative flow plot, and (**E**) quantification of the frequency of *Mtb* infection among lung wild-type CD45.1^{+} and *Il1r1*$^{-/-}$ CD45.1^{-} IMs (n = 8) 25 days post-infection. (**F**) Experimental setup and (**G**) lung bacterial burden of bone marrow chimera mice with wild-type neurons (CD45.1 host, n = 13), littermate control neurons (Adv$^{+/+}$ Il1r1$^{fl/fl}$ host, n = 9), and IL-1 receptor-deficient neurons (Adv$^{Cre/+}$ Il1r1$^{fl/fl}$ host, n = 14) 25 days after *Mtb* infection. Pooled data from two independent experiments is shown in (E) and (G). Statistical significance in (E) was calculated with a paired t test and in (G) with a one-way ANOVA with Tukey's multiple comparison test.

Supplementary Figure 8. Classifying T cell, ILC, and stromal cell scRNA-seq clusters. Dot plot of lineage of markers used to annotate the clusters in our (**A**) T cell dataset, (**B**) ILC dataset, and (**C**) stromal cell dataset**.**

Supplementary Figure 9. NicheNet analysis of IL-1 regulated ligands that could activate interstitial macrophages. (**A**) List of IL-1 regulated potential ligands identified in stromal and hematopoietic cells. (**B**) Receptor expression on interstitial macrophages for the IL-1-regulated ligands. (**C**) Predicted ligand activity based on genes differently expressed by the activated interstitial macrophage subsets.

References

1. WHO. Global Tuberculosis Report 2024. https://www.who.int/teams/global-tuberculosis-programme/tb-reports/global-tuberculosis-report-2024.
2. Davenne, T. & McShane, H. Why don't we have an effective tuberculosis vaccine yet? *Expert Rev Vaccines* **15**, 1009–1013 (2016).
3. Cooper, A. M. *et al.* Disseminated tuberculosis in interferon gamma gene-disrupted mice. *J Exp Med* **178**, 2243–2247 (1993).
4. Flynn, J. L. *et al.* An essential role for interferon gamma in resistance to Mycobacterium tuberculosis infection. *J Exp Med* **178**, 2249–2254 (1993).
5. Flynn, J. L. *et al.* Tumor necrosis factor-alpha is required in the protective immune response against Mycobacterium tuberculosis in mice. *Immunity* **2**, 561–572 (1995).
6. Cohen, S. B., Gern, B. H. & Urdahl, K. B. The Tuberculous Granuloma and Preexisting Immunity. *Annual Review of Immunology* **40**, 589–614 (2022).
7. Russell, D. G., Barry, C. E. & Flynn, J. L. Tuberculosis: What We Don't Know Can, and Does, Hurt Us. *Science* **328**, 852–856 (2010).
8. Berry, M. P. R. *et al.* An interferon-inducible neutrophil-driven blood transcriptional signature in human tuberculosis. *Nature* **466**, 973–977 (2010).
9. Saqib, M. *et al.* Hematopoietic dysregulation caused by neutrophils underlies impaired T-cell response and enhanced susceptibility to tuberculosis. Preprint at https://doi.org/10.21203/rs.3.rs-2921835/v1 (2023).

10. McNab, F. W. *et al.* TPL-2-ERK1/2 signaling promotes host resistance against intracellular bacterial infection by negative regulation of type I IFN production. *J Immunol* **191**, 1732–1743 (2013).
11. Moreira-Teixeira, L. *et al.* T Cell-Derived IL-10 Impairs Host Resistance to Mycobacterium tuberculosis Infection. *J Immunol* **199**, 613–623 (2017).
12. Stanley, S. A., Johndrow, J. E., Manzanillo, P. & Cox, J. S. The Type I IFN response to infection with Mycobacterium tuberculosis requires ESX-1-mediated secretion and contributes to pathogenesis. *J Immunol* **178**, 3143–3152 (2007).
13. Mishra, B. B. *et al.* Nitric oxide prevents a pathogen permissive granulocytic inflammation during tuberculosis. *Nat Microbiol* **2**, 17072 (2017).
14. Ji, D. X. *et al.* Role of the transcriptional regulator SP140 in resistance to bacterial infections via repression of type I interferons. *eLife* **10**, e67290 (2021).
15. Kotov, D. I. *et al.* Early cellular mechanisms of type I interferon-driven susceptibility to tuberculosis. *Cell* **186**, 5536-5553.e22 (2023).
16. Witt, K. C. *et al.* The SP140-RESIST pathway regulates interferon mRNA stability and antiviral immunity. 2024.08.28.610186 Preprint at https://doi.org/10.1101/2024.08.28.610186 (2024).
17. Ji, D. X. *et al.* Type I interferon-driven susceptibility to Mycobacterium tuberculosis is mediated by interleukin-1 receptor antagonist IL-1Ra. *Nat Microbiol* **4**, 2128–2135 (2019).
18. Pichugin, A. V., Yan, B.-S., Sloutsky, A., Kobzik, L. & Kramnik, I. Dominant role of the sst1 locus in pathogenesis of necrotizing lung granulomas during chronic tuberculosis infection and reactivation in genetically resistant hosts. *Am J Pathol* **174**, 2190–2201 (2009).
19. Pan, H. *et al.* Ipr1 gene mediates innate immunity to tuberculosis. *Nature* **434**, 767–772 (2005).
20. MacMicking, J. D. *et al.* Identification of nitric oxide synthase as a protective locus against tuberculosis. *Proc Natl Acad Sci U S A* **94**, 5243–5248 (1997).
21. Nair, S. *et al.* Irg1 expression in myeloid cells prevents immunopathology during M. tuberculosis infection. *Journal of Experimental Medicine* **215**, 1035–1045 (2018).
22. Moreira-Teixeira, L. *et al.* Type I IFN exacerbates disease in tuberculosis-susceptible mice by inducing neutrophil-mediated lung inflammation and NETosis. *Nat Commun* **11**, 5566 (2020).
23. Bohrer, A. C., Tocheny, C., Assmann, M., Ganusov, V. V. & Mayer-Barber, K. D. Cutting Edge: IL-1R1 Mediates Host Resistance to Mycobacterium tuberculosis by Trans-Protection of Infected Cells. *J Immunol* **201**, 1645–1650 (2018).
24. Eruslanov, E. B. *et al.* Neutrophil Responses to Mycobacterium tuberculosis Infection in Genetically Susceptible and Resistant Mice. *Infect Immun* **73**, 1744–1753 (2005).
25. Mattila, J. T., Maiello, P., Sun, T., Via, L. E. & Flynn, J. L. Granzyme B-expressing neutrophils correlate with bacterial load in granulomas from Mycobacterium tuberculosis-infected cynomolgus macaques. *Cell Microbiol* **17**, 1085–1097 (2015).
26. Gideon, H. P., Phuah, J., Junecko, B. A. & Mattila, J. T. Neutrophils express pro- and anti-inflammatory cytokines in granulomas from Mycobacterium tuberculosis-infected cynomolgus macaques. *Mucosal Immunol* **12**, 1370–1381 (2019).
27. Meier, S. *et al.* Neutrophil degranulation, NETosis and platelet degranulation pathway genes are co-induced in whole blood up to six months before tuberculosis diagnosis. *PLoS One* **17**, e0278295 (2022).

28. Eum, S.-Y. *et al.* Neutrophils are the predominant infected phagocytic cells in the airways of patients with active pulmonary TB. *Chest* **137**, 122–128 (2010).
29. Lovewell, R. R., Baer, C. E., Mishra, B. B., Smith, C. M. & Sassetti, C. M. Granulocytes act as a niche for Mycobacterium tuberculosis growth. *Mucosal Immunol* **14**, 229–241 (2021).
30. Dallenga, T. *et al.* M. tuberculosis-Induced Necrosis of Infected Neutrophils Promotes Bacterial Growth Following Phagocytosis by Macrophages. *Cell Host Microbe* **22**, 519-530.e3 (2017).
31. Chowdhury, C. S. *et al.* Type I IFN signaling mediates NET release to promote Mycobacterium tuberculosis replication and granuloma caseation. 2022.11.29.518376 Preprint at https://doi.org/10.1101/2022.11.29.518376 (2022).
32. Herrero-Cervera, A., Soehnlein, O. & Kenne, E. Neutrophils in chronic inflammatory diseases. *Cell Mol Immunol* **19**, 177–191 (2022).
33. Mishra, B. B. *et al.* Nitric oxide controls the immunopathology of tuberculosis by inhibiting NLRP3 inflammasome-dependent processing of IL-1β. *Nat Immunol* **14**, 52–60 (2013).
34. Law, K. *et al.* Increased release of interleukin-1 beta, interleukin-6, and tumor necrosis factor-alpha by bronchoalveolar cells lavaged from involved sites in pulmonary tuberculosis. *Am J Respir Crit Care Med* **153**, 799–804 (1996).
35. Zhang, G. *et al.* Allele-specific induction of IL-1β expression by C/EBPβ and PU.1 contributes to increased tuberculosis susceptibility. *PLoS Pathog* **10**, e1004426 (2014).
36. Mayer-Barber, K. D. *et al.* Host-directed therapy of tuberculosis based on interleukin-1 and type I interferon crosstalk. *Nature* **511**, 99–103 (2014).
37. Mayer-Barber, K. D. *et al.* Cutting Edge: Caspase-1 Independent IL-1β Production Is Critical for Host Resistance to Mycobacterium tuberculosis and Does Not Require TLR Signaling In Vivo. *J Immunol* **184**, 3326–3330 (2010).
38. Mayer-Barber, K. D. *et al.* Innate and Adaptive Interferons Suppress IL-1α and IL-1β Production by Distinct Pulmonary Myeloid Subsets during Mycobacterium tuberculosis Infection. *Immunity* **35**, 1023–1034 (2011).
39. Di Paolo, N. C. *et al.* Interdependence between interleukin-1 and tumor necrosis factor controls TNF-dependent effector functions during Mycobacterium tuberculosis infection. *Immunity* **43**, 1125–1136 (2015).
40. Juffermans, N. P. *et al.* Interleukin-1 Signaling Is Essential for Host Defense during Murine Pulmonary Tuberculosis. *The Journal of Infectious Diseases* **182**, 902–908 (2000).
41. Bloom, C. I. *et al.* Detectable Changes in The Blood Transcriptome Are Present after Two Weeks of Antituberculosis Therapy. *PLOS ONE* **7**, e46191 (2012).
42. Blankley, S. *et al.* A 380-gene meta-signature of active tuberculosis compared with healthy controls. *European Respiratory Journal* **47**, 1873–1876 (2016).
43. Kwan, P. K. W. *et al.* A blood RNA transcript signature for TB exposure in household contacts. *BMC Infectious Diseases* **20**, 403 (2020).
44. Kimmey, J. M. *et al.* Unique role for ATG5 in PMN-mediated immunopathology during M. tuberculosis infection. *Nature* **528**, 565–569 (2015).
45. Yeremeev, V., Linge, I., Kondratieva, T. & Apt, A. Neutrophils exacerbate tuberculosis infection in genetically susceptible mice. *Tuberculosis (Edinb)* **95**, 447–451 (2015).
46. Huynh, J. P. *et al.* Bhlhe40 is an essential repressor of IL-10 during Mycobacterium tuberculosis infection. *Journal of Experimental Medicine* **215**, 1823–1838 (2018).

47. Hao, Y. *et al.* Integrated analysis of multimodal single-cell data. *Cell* **184**, 3573-3587.e29 (2021).
48. Stoeckius, M. *et al.* Simultaneous epitope and transcriptome measurement in single cells. *Nat Methods* **14**, 865–868 (2017).
49. Eckold, C. *et al.* Impact of Intermediate Hyperglycemia and Diabetes on Immune Dysfunction in Tuberculosis. *Clin Infect Dis* **72**, 69–78 (2020).
50. Singhania, A. *et al.* A modular transcriptional signature identifies phenotypic heterogeneity of human tuberculosis infection. *Nat Commun* **9**, 2308 (2018).
51. Bloom, C. I. *et al.* Transcriptional Blood Signatures Distinguish Pulmonary Tuberculosis, Pulmonary Sarcoidosis, Pneumonias and Lung Cancers. *PLOS ONE* **8**, e70630 (2013).
52. Marcovecchio, P. M., Thomas, G. & Salek-Ardakani, S. CXCL9-expressing tumor-associated macrophages: new players in the fight against cancer. *J Immunother Cancer* **9**, e002045 (2021).
53. Matsubara, E. *et al.* SPP1 Derived from Macrophages Is Associated with a Worse Clinical Course and Chemo-Resistance in Lung Adenocarcinoma. *Cancers (Basel)* **14**, 4374 (2022).
54. Bill, R. *et al.* CXCL9:SPP1 macrophage polarity identifies a network of cellular programs that control human cancers. *Science* **381**, 515–524 (2023).
55. Wang, D. *et al.* The association between osteopontin and tuberculosis: A systematic review and meta-analysis. *PLoS One* **15**, e0242702 (2020).
56. Yang, Q. *et al.* The interaction of macrophages and CD8 T cells in bronchoalveolar lavage fluid is associated with latent tuberculosis infection. *Emerging Microbes & Infections* **12**, 2239940 (2023).
57. Katano, H., Hebisawa, A., Sato, Y. & Hoshino, Y. Identification of SPP1-positive macrophages by single-cell spatial analysis in human lung tissues with mycobacterial infection. 2024.09.12.612778 Preprint at https://doi.org/10.1101/2024.09.12.612778 (2025).
58. McColl, S. R., Paquin, R., Ménard, C. & Beaulieu, A. D. Human neutrophils produce high levels of the interleukin 1 receptor antagonist in response to granulocyte/macrophage colony-stimulating factor and tumor necrosis factor alpha. *Journal of Experimental Medicine* **176**, 593–598 (1992).
59. Winchell, C. G. *et al.* CD8+ lymphocytes are critical for early control of tuberculosis in macaques. *Journal of Experimental Medicine* **220**, e20230707 (2023).
60. Zhou, T. *et al.* IL-18BP is a secreted immune checkpoint and barrier to IL-18 immunotherapy. *Nature* **583**, 609–614 (2020).
61. Jiang, X. *et al.* Role of the tumor microenvironment in PD-L1/PD-1-mediated tumor immune escape. *Molecular Cancer* **18**, 10 (2019).
62. Mittal, S. K., Cho, K.-J., Ishido, S. & Roche, P. A. Interleukin 10 (IL-10)-mediated Immunosuppression. *J Biol Chem* **290**, 27158–27167 (2015).
63. Zak, D. E. *et al.* A blood RNA signature for tuberculosis disease risk: a prospective cohort study. *The Lancet* **387**, 2312–2322 (2016).
64. Scriba, T. J. *et al.* Sequential inflammatory processes define human progression from M. tuberculosis infection to tuberculosis disease. *PLOS Pathogens* **13**, e1006687 (2017).
65. Yu, J. *et al.* Early-stage idiopathic pulmonary fibrosis is characterized by bronchoalveolar accumulation of SPP1+ macrophages. 2023.12.06.569201 Preprint at https://doi.org/10.1101/2023.12.06.569201 (2023).

66. Gander-Bui, H. T. T. *et al.* Targeted removal of macrophage-secreted interleukin-1 receptor antagonist protects against lethal Candida albicans sepsis. *Immunity* **56**, 1743-1760.e9 (2023).
67. Scott, C. L. *et al.* The Transcription Factor ZEB2 Is Required to Maintain the Tissue-Specific Identities of Macrophages. *Immunity* **49**, 312-325.e5 (2018).
68. Lamacchia, C., Palmer, G., Seemayer, C. A., Talabot-Ayer, D. & Gabay, C. Enhanced Th1 and Th17 responses and arthritis severity in mice with a deficiency of myeloid cell–specific interleukin-1 receptor antagonist. *Arthritis & Rheumatism* **62**, 452–462 (2010).
69. Jain, A., Song, R., Wakeland, E. K. & Pasare, C. T cell-intrinsic IL-1R signaling licenses effector cytokine production by memory CD4 T cells. *Nat Commun* **9**, 3185 (2018).
70. Ohne, Y. *et al.* IL-1 is a critical regulator of group 2 innate lymphoid cell function and plasticity. *Nat Immunol* **17**, 646–655 (2016).
71. Zhou, L. *et al.* Innate lymphoid cells support regulatory T cells in the intestine through interleukin-2. *Nature* **568**, 405–409 (2019).
72. Browaeys, R., Saelens, W. & Saeys, Y. NicheNet: modeling intercellular communication by linking ligands to target genes. *Nat Methods* **17**, 159–162 (2020).
73. Mailhot, B. *et al.* Neuronal interleukin-1 receptors mediate pain in chronic inflammatory diseases. *J Exp Med* **217**, e20191430 (2020).
74. Liu, X. *et al.* Cell-Type-Specific Interleukin 1Receptor 1 Signaling in the Brain Regulates Distinct Neuroimmune Activities. *Immunity* **50**, 317-333.e6 (2019).
75. Hurskainen, M. *et al.* Single cell transcriptomic analysis of murine lung development on hyperoxia-induced damage. *Nat Commun* **12**, 1565 (2021).
76. Huang, L., Nazarova, E. V., Tan, S., Liu, Y. & Russell, D. G. Growth of Mycobacterium tuberculosis in vivo segregates with host macrophage metabolism and ontogeny. *Journal of Experimental Medicine* **215**, 1135–1152 (2018).
77. Ardain, A. *et al.* Group 3 innate lymphoid cells mediate early protective immunity against tuberculosis. *Nature* **570**, 528–532 (2019).
78. Gopal, R. *et al.* Unexpected Role for IL-17 in Protective Immunity against Hypervirulent Mycobacterium tuberculosis HN878 Infection. *PLOS Pathogens* **10**, e1004099 (2014).
79. Van Dis, E. *et al.* STING-Activating Adjuvants Elicit a Th17 Immune Response and Protect against Mycobacterium tuberculosis Infection. *Cell Rep* **23**, 1435–1447 (2018).
80. Jong, R. M. *et al.* Mucosal Vaccination with Cyclic Dinucleotide Adjuvants Induces Effective T Cell Homing and IL-17-Dependent Protection against Mycobacterium tuberculosis Infection. *J Immunol* **208**, 407–419 (2022).
81. Alcorn, J. F. IL-22 Plays a Critical Role in Maintaining Epithelial Integrity During Pulmonary Infection. *Front Immunol* **11**, 1160 (2020).
82. Coussens, L. M. & Werb, Z. Inflammation and cancer. *Nature* **420**, 860–867 (2002).
83. Ostrand-Rosenberg, S. & Sinha, P. Myeloid-Derived Suppressor Cells: Linking Inflammation and Cancer. *J Immunol* **182**, 4499–4506 (2009).
84. Barbosa Bomfim, C. C. *et al.* Harmful Effects of Granulocytic Myeloid-Derived Suppressor Cells on Tuberculosis Caused by Hypervirulent Mycobacteria. *J Infect Dis* **223**, 494–507 (2021).
85. Tsiganov, E. N. *et al.* Gr-1dimCD11b+ immature myeloid-derived suppressor cells but not neutrophils are markers of lethal tuberculosis infection in mice. *J Immunol* **192**, 4718–4727 (2014).

86. La Manna, M. P. *et al.* Mycobacterium tuberculosis Drives Expansion of Low-Density Neutrophils Equipped With Regulatory Activities. *Front Immunol* **10**, 2761 (2019).
87. Knaul, J. K. *et al.* Lung-residing myeloid-derived suppressors display dual functionality in murine pulmonary tuberculosis. *Am J Respir Crit Care Med* **190**, 1053–1066 (2014).
88. Huang, B. *et al.* Gr-1+CD115+ immature myeloid suppressor cells mediate the development of tumor-induced T regulatory cells and T-cell anergy in tumor-bearing host. *Cancer Res* **66**, 1123–1131 (2006).
89. du Plessis, N. *et al.* Increased frequency of myeloid-derived suppressor cells during active tuberculosis and after recent mycobacterium tuberculosis infection suppresses T-cell function. *Am J Respir Crit Care Med* **188**, 724–732 (2013).
90. Singh, B. *et al.* Myeloid-Derived Suppressor Cells Mediate T Cell Dysfunction in Nonhuman Primate TB Granulomas. *mBio* **12**, e0318921 (2021).
91. Ashenafi, S. & Brighenti, S. Reinventing the human tuberculosis (TB) granuloma: Learning from the cancer field. *Front Immunol* **13**, 1059725 (2022).
92. Gern, B. H. *et al.* TGFβ restricts expansion, survival, and function of T cells within the tuberculous granuloma. *Cell Host & Microbe* **29**, 594-606.e6 (2021).
93. McCaffrey, E. F. *et al.* The immunoregulatory landscape of human tuberculosis granulomas. *Nat Immunol* **23**, 318–329 (2022).
94. Barber, D. L., Mayer-Barber, K. D., Feng, C. G., Sharpe, A. H. & Sher, A. CD4 T cells promote rather than control tuberculosis in the absence of PD-1-mediated inhibition. *J Immunol* **186**, 1598–1607 (2011).
95. Kauffman, K. D. *et al.* PD-1 blockade exacerbates Mycobacterium tuberculosis infection in rhesus macaques. *Sci Immunol* **6**, eabf3861 (2021).
96. Blumenthal, A. *et al.* M. tuberculosis Induces Potent Activation of IDO-1, but This Is Not Essential for the Immunological Control of Infection. *PLoS One* **7**, e37314 (2012).
97. Gautam, U. S. *et al.* In vivo inhibition of tryptophan catabolism reorganizes the tuberculoma and augments immune-mediated control of Mycobacterium tuberculosis. *Proceedings of the National Academy of Sciences* **115**, E62–E71 (2018).
98. Singh, B. *et al.* Inhibition of indoleamine dioxygenase leads to better control of tuberculosis adjunctive to chemotherapy. *JCI Insight* **8**, e163101.
99. Jung, Y.-J., Ryan, L., LaCourse, R. & North, R. J. Increased interleukin-10 expression is not responsible for failure of T helper 1 immunity to resolve airborne Mycobacterium tuberculosis infection in mice. *Immunology* **109**, 295–299 (2003).
100. North, R. J. Mice incapable of making IL-4 or IL-10 display normal resistance to infection with Mycobacterium tuberculosis. *Clinical and Experimental Immunology* **113**, 55–58 (1998).
101. Higgins, D. M. *et al.* Lack of IL-10 alters inflammatory and immune responses during pulmonary Mycobacterium tuberculosis infection. *Tuberculosis* **89**, 149–157 (2009).
102. Beamer, G. L. *et al.* Interleukin-10 Promotes Mycobacterium tuberculosis Disease Progression in CBA/J Mice1. *The Journal of Immunology* **181**, 5545–5550 (2008).
103. Redford, P. S. *et al.* Enhanced protection to Mycobacterium tuberculosis infection in IL-10-deficient mice is accompanied by early and enhanced Th1 responses in the lung. *European Journal of Immunology* **40**, 2200–2210 (2010).
104. Martinez, L. *et al.* Cytomegalovirus acquisition in infancy and the risk of tuberculosis disease in childhood: a longitudinal birth cohort study in Cape Town, South Africa. *The Lancet Global Health* **9**, e1740–e1749 (2021).

105. Müller, J. *et al.* Cytomegalovirus infection is a risk factor for tuberculosis disease in infants. *JCI Insight* **4**, 130090 (2019).
106. Walaza, S. *et al.* Influenza virus infection is associated with increased risk of death amongst patients hospitalized with confirmed pulmonary tuberculosis in South Africa, 2010–2011. *BMC Infectious Diseases* **15**, 26 (2015).
107. Antonelli, L. R. V. *et al.* Intranasal Poly-IC treatment exacerbates tuberculosis in mice through the pulmonary recruitment of a pathogen-permissive monocyte/macrophage population. *J Clin Invest* **120**, 1674–1682 (2010).
108. Kang, T. G. *et al.* Viral coinfection promotes tuberculosis immunopathogenesis by type I IFN signaling-dependent impediment of Th1 cell pulmonary influx. *Nat Commun* **13**, 3155 (2022).
109. Redford, P. S. *et al.* Influenza A Virus Impairs Control of Mycobacterium tuberculosis Coinfection Through a Type I Interferon Receptor–Dependent Pathway. *J Infect Dis* **209**, 270–274 (2014).
110. Volkert, M., Pierce, C., Horsfall, F. L. & Dubos, R. J. THE ENHANCING EFFECT OF CONCURRENT INFECTION WITH PNEUMOTROPIC VIRUSES ON PULMONARY TUBERCULOSIS IN MICE. *J Exp Med* **86**, 203–214 (1947).
111. Xu, W. *et al.* Early innate and adaptive immune perturbations determine long-term severity of chronic virus and Mycobacterium tuberculosis coinfection. *Immunity* **54**, 526-541.e7 (2021).
112. Ring, S. *et al.* Blocking IL-10 receptor signaling ameliorates Mycobacterium tuberculosis infection during influenza-induced exacerbation. *JCI Insight* **5**, e126533, 126533 (2019).
113. MacDonald, L. *et al.* COVID-19 and RA share an SPP1 myeloid pathway that drives PD-L1+ neutrophils and CD14+ monocytes. *JCI Insight* **6**, e147413.
114. Dinarello, C. A. Overview of the IL-1 family in innate inflammation and acquired immunity. *Immunol Rev* **281**, 8–27 (2018).
115. Chensue, S. W., Warmington, K. S., Berger, A. E. & Tracey, D. E. Immunohistochemical demonstration of interleukin-1 receptor antagonist protein and interleukin-1 in human lymphoid tissue and granulomas. *Am J Pathol* **140**, 269–275 (1992).
116. Settas, L. D., Tsimirikas, G., Vosvotekas, G., Triantafyllidou, E. & Nicolaides, P. Reactivation of pulmonary tuberculosis in a patient with rheumatoid arthritis during treatment with IL-1 receptor antagonists (anakinra). *J Clin Rheumatol* **13**, 219–220 (2007).
117. Winchell, C. G. *et al.* Evaluation of IL-1 Blockade as an Adjunct to Linezolid Therapy for Tuberculosis in Mice and Macaques. *Frontiers in Immunology* **11**, (2020).
118. Liu, X., Boyer, M. A., Holmgren, A. M. & Shin, S. Legionella-Infected Macrophages Engage the Alveolar Epithelium to Metabolically Reprogram Myeloid Cells and Promote Antibacterial Inflammation. *Cell Host Microbe* **28**, 683-698.e6 (2020).
119. Rothchild, A. C. *et al.* Role of Granulocyte-Macrophage Colony-Stimulating Factor Production by T Cells during Mycobacterium tuberculosis Infection. *mBio* **8**, 10.1128/mbio.01514-17 (2017).
120. Gonzalez-Juarrero, M. *et al.* Disruption of granulocyte macrophage-colony stimulating factor production in the lungs severely affects the ability of mice to control Mycobacterium tuberculosis infection. *J Leukoc Biol* **77**, 914–922 (2005).
121. Dis, E. V. *et al.* IFN-γ-independent control of M. tuberculosis requires CD4 T cell-derived GM-CSF and activation of HIF-1α. *PLOS Pathogens* **18**, e1010721 (2022).

122. Mayer-Barber, K. D. Granulocytes subsets and their divergent functions in host resistance to Mycobacterium tuberculosis - a 'tipping-point' model of disease exacerbation. *Curr Opin Immunol* **84**, 102365 (2023).
123. Müller, U. *et al.* Functional role of type I and type II interferons in antiviral defense. *Science* **264**, 1918–1921 (1994).
124. Shen, F. W. *et al.* Cloning of Ly-5 cDNA. *Proc Natl Acad Sci U S A* **82**, 7360–7363 (1985).
125. Glaccum, M. B. *et al.* Phenotypic and functional characterization of mice that lack the type I receptor for IL-1. *J Immunol* **159**, 3364–3371 (1997).
126. Robson, M. J. *et al.* Generation and Characterization of Mice Expressing a Conditional Allele of the Interleukin-1 Receptor Type 1. *PLoS One* **11**, e0150068 (2016).
127. Zhou, X. *et al.* Deletion of PIK3C3/Vps34 in sensory neurons causes rapid neurodegeneration by disrupting the endosomal but not the autophagic pathway. *Proc Natl Acad Sci U S A* **107**, 9424–9429 (2010).
128. Laubach, V. E., Shesely, E. G., Smithies, O. & Sherman, P. A. Mice lacking inducible nitric oxide synthase are not resistant to lipopolysaccharide-induced death. *Proc Natl Acad Sci U S A* **92**, 10688–10692 (1995).
129. Takaki, K., Davis, J. M., Winglee, K. & Ramakrishnan, L. Evaluation of the pathogenesis and treatment of Mycobacterium marinum infection in zebrafish. *Nat Protoc* **8**, 1114–1124 (2013).
130. Kotov, D. I., Pengo, T., Mitchell, J. S., Gastinger, M. J. & Jenkins, M. K. Chrysalis: A New Method for High-Throughput Histo-Cytometry Analysis of Images and Movies. *The Journal of Immunology* **202**, 300–308 (2019).
131. Gerner, M. Y., Kastenmuller, W., Ifrim, I., Kabat, J. & Germain, R. N. Histo-cytometry: a method for highly multiplex quantitative tissue imaging analysis applied to dendritic cell subset microanatomy in lymph nodes. *Immunity* **37**, 364–376 (2012).
132. Anderson, K. G. *et al.* Intravascular staining for discrimination of vascular and tissue leukocytes. *Nat Protoc* **9**, 209–222 (2014).
133. Stoeckius, M. *et al.* Cell Hashing with barcoded antibodies enables multiplexing and doublet detection for single cell genomics. *Genome Biology* **19**, 224 (2018).
134. Roelli, P., bbimber, Flynn, B., santiagorevale & Gui, G. Hoohm/CITE-seq-Count: 1.4.2. Zenodo https://doi.org/10.5281/zenodo.2590196 (2019).
135. Andreatta, M. & Carmona, S. J. UCell: Robust and scalable single-cell gene signature scoring. *Comput Struct Biotechnol J* **19**, 3796–3798 (2021).
136. R Core Team. R: A language and environment for statistical computing. R Foundation for Statistical Computing (2021).
137. Foroutan, M. *et al.* Single sample scoring of molecular phenotypes. *BMC Bioinformatics* **19**, 404 (2018).
138. Robin, X. *et al.* pROC: an open-source package for R and S+ to analyze and compare ROC curves. *BMC Bioinformatics* **12**, 77 (2011).
139. Love, M. I., Huber, W. & Anders, S. Moderated estimation of fold change and dispersion for RNA-seq data with DESeq2. *Genome Biol* **15**, 550 (2014).

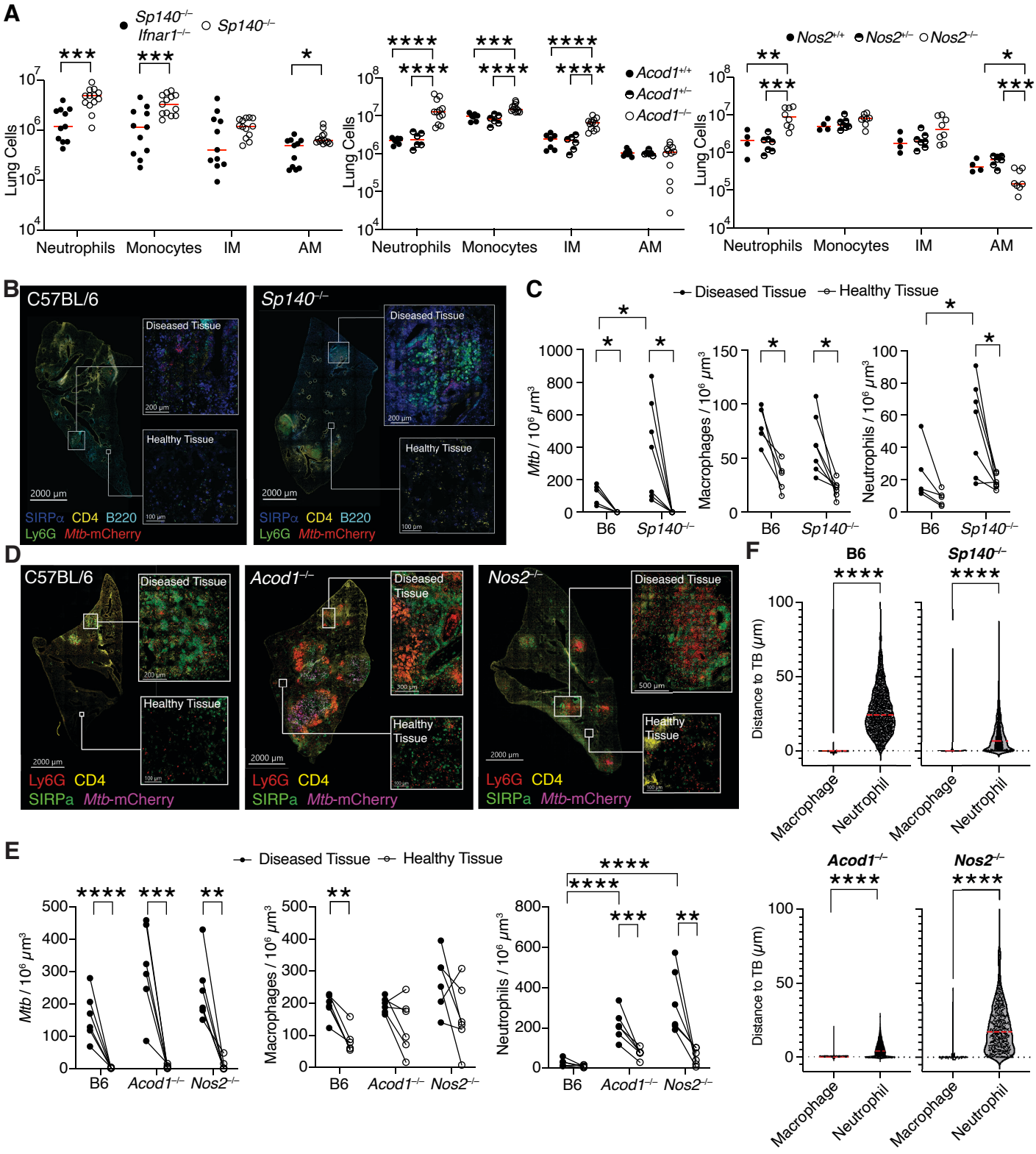

Figure 1.

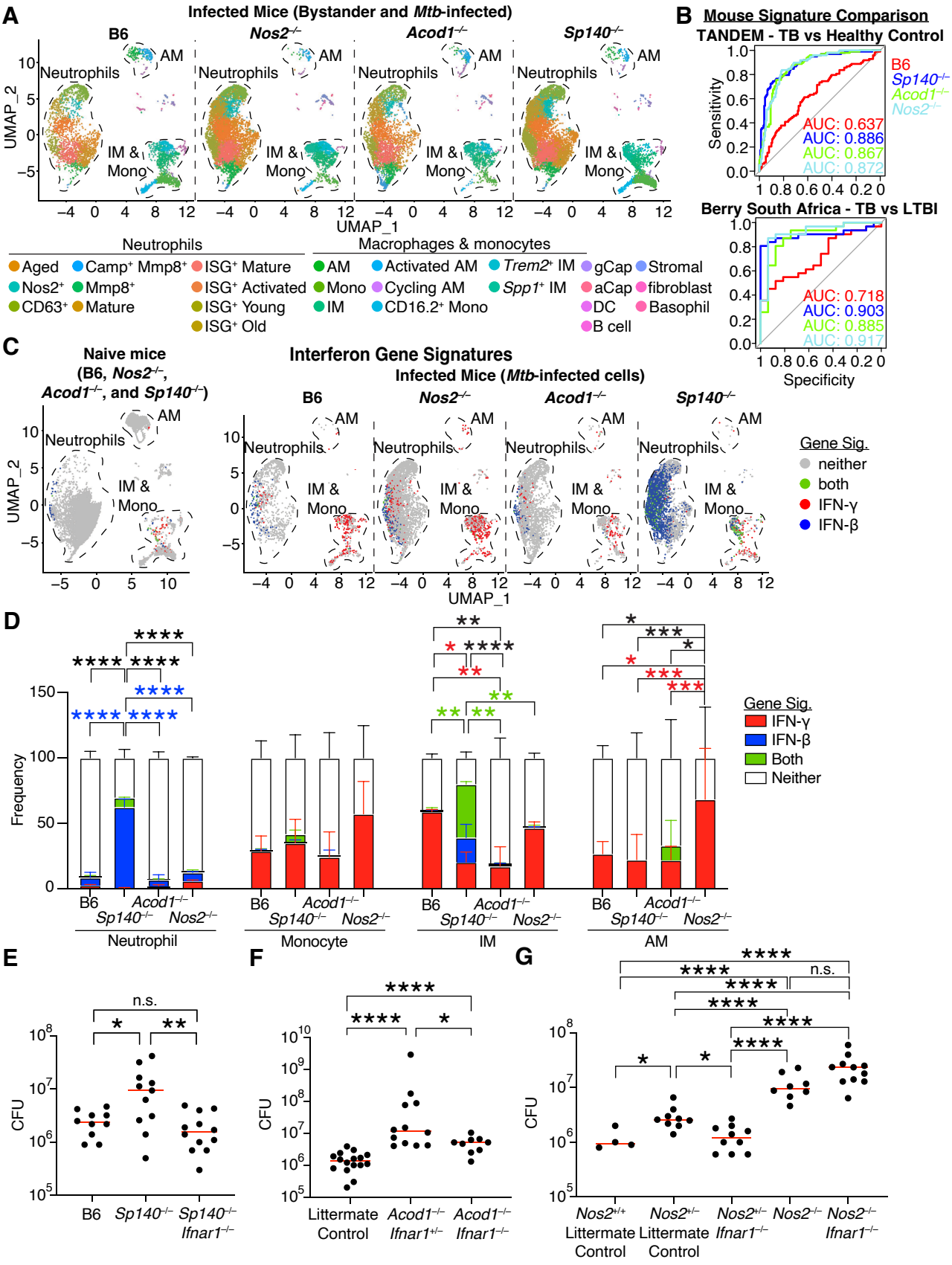

Figure 2.

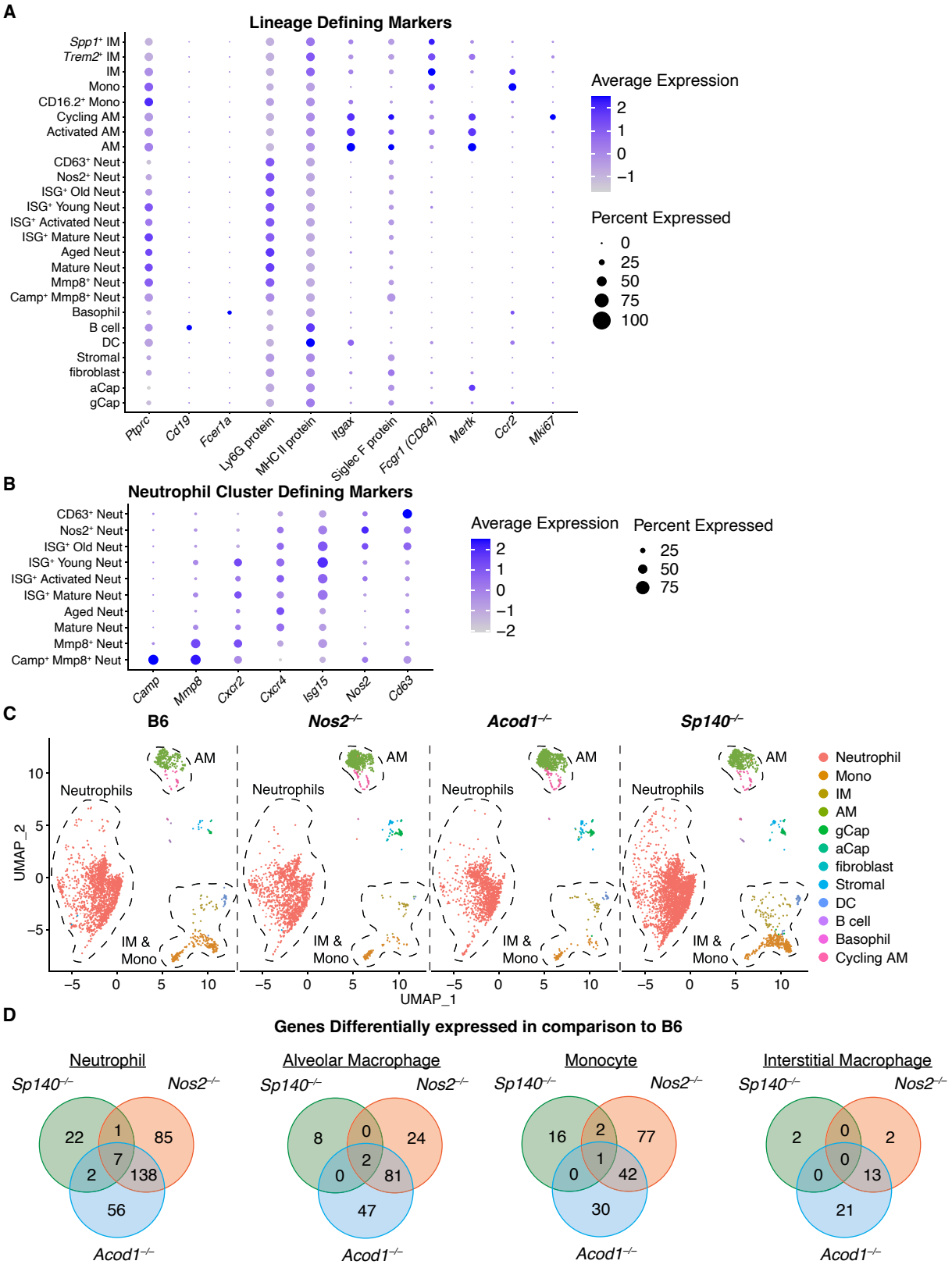

Supplementary Figure 1.

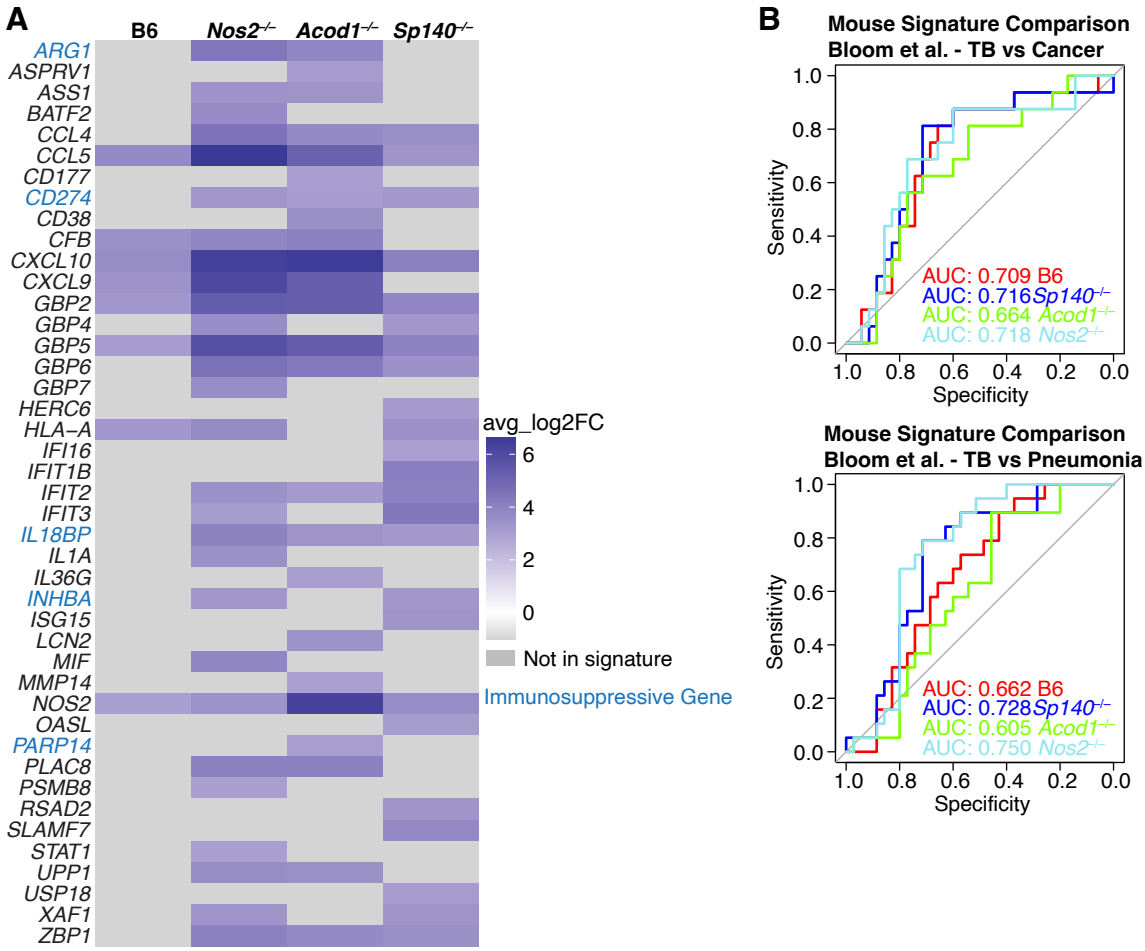

Supplementary Figure 2.

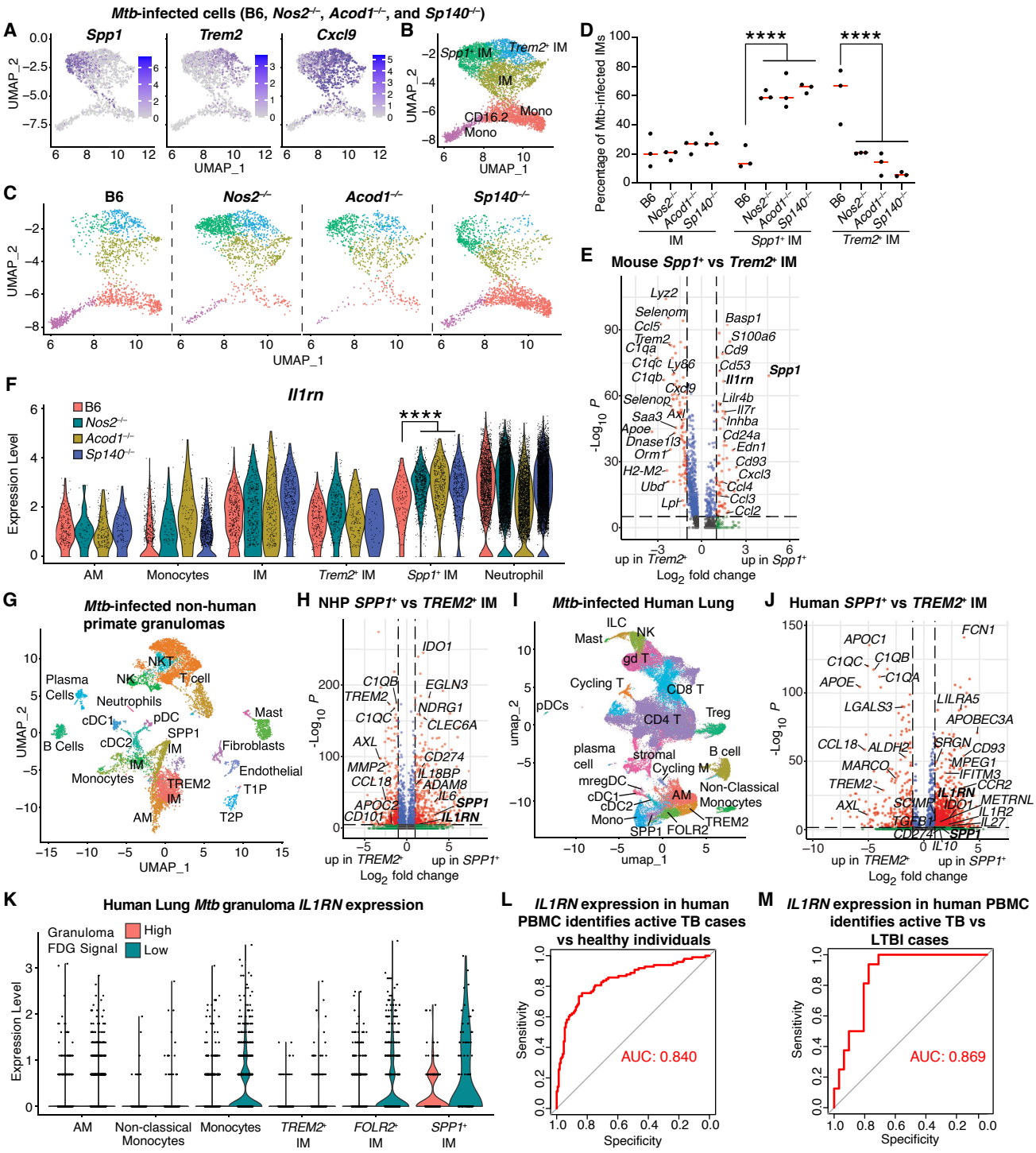

Figure 3.

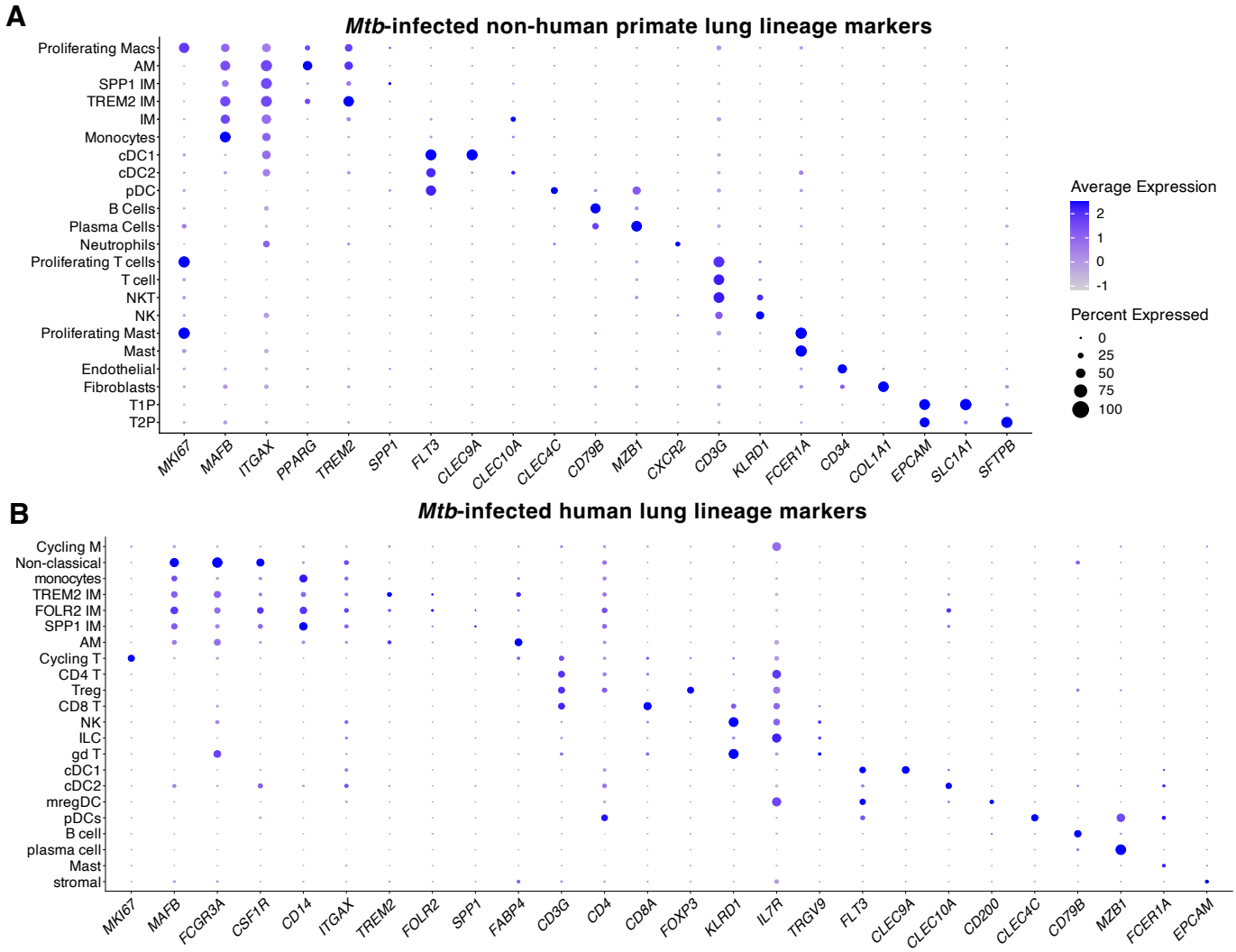

Supplementary Figure 3.

A

Mouse genes upregulated by *Spp1*⁺ IM relative to *Trem2*⁺ IM

Upregulated genes conserved between mouse and human

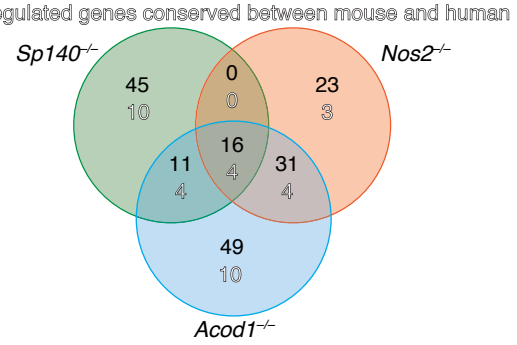

	Sp140$^{-/-}$	*Nos2*$^{-/-}$	*Acod1*$^{-/-}$
Mouse genes:	72	70	107
Overlap with human SPP1⁺ IMs (genes):	18 (25%)	11 (16%)	22 (21%)

B

Core *Spp1*⁺ IM genes

- *Upp1*
- *S100a6*
- *Inhba*
- *Cd9*
- *AA467197*
- *Anxa2*
- *Fam129b*
- *Hilpda*
- *Cd24a*
- *Lilrb4*
- *Basp1*
- *Spp1*

Conserved across 3 mouse genotypes

- *Il1rn*
- *Srgn*
- *Metrnl*
- *Scimp*

Conserved across 3 mouse genotypes and humans

Supplementary Figure 4.

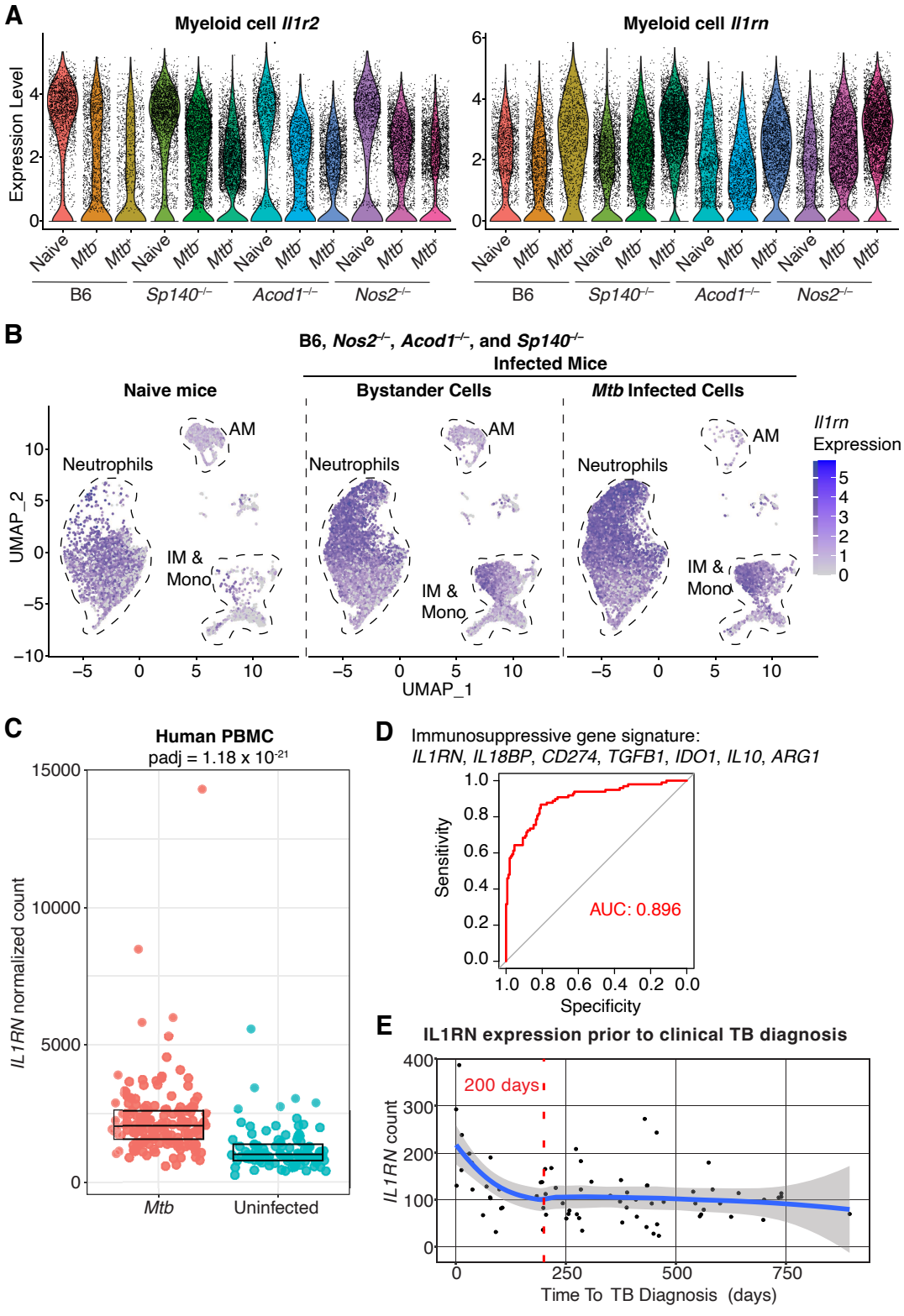

Supplementary Figure 5.

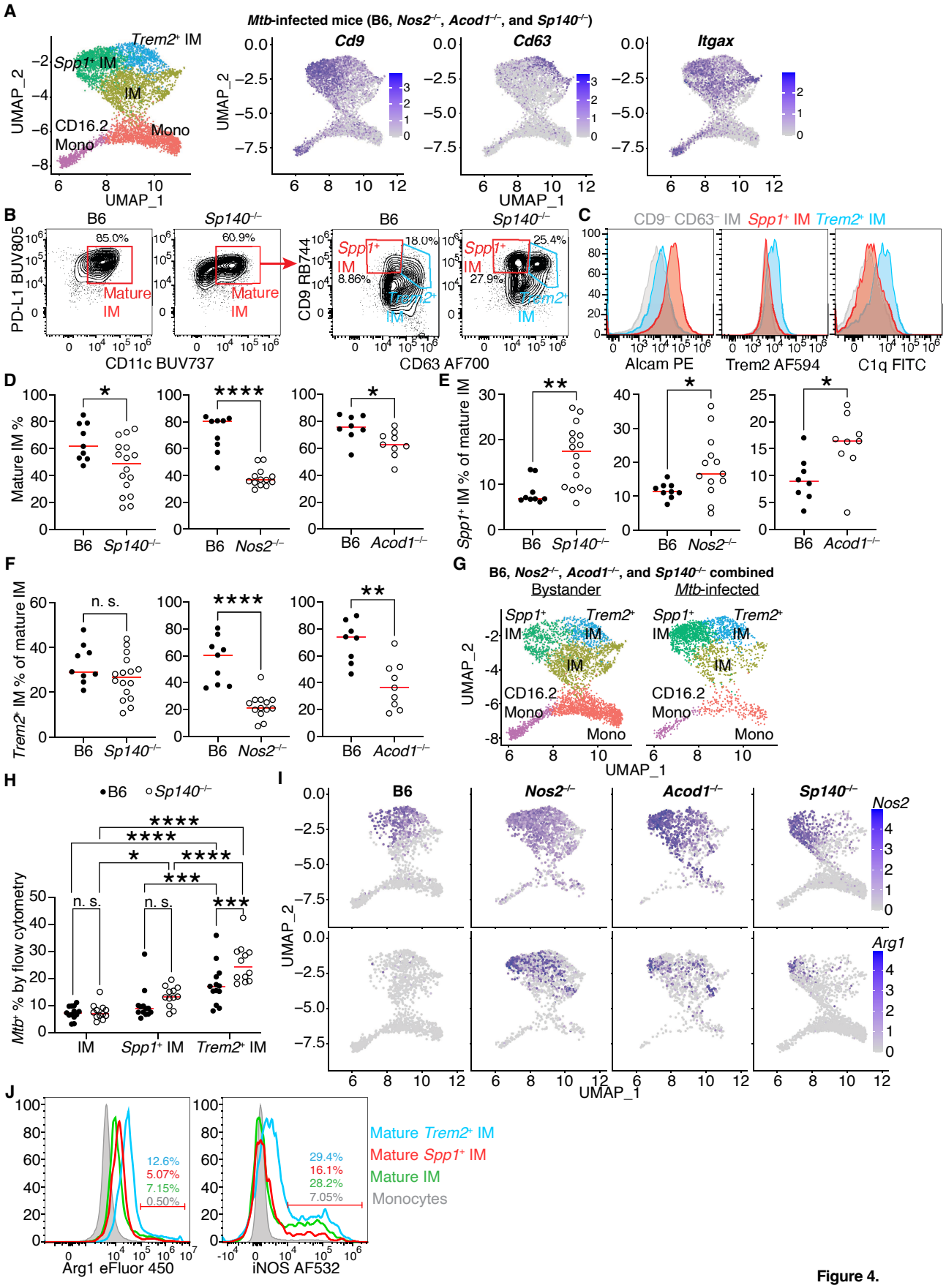

Figure 4.

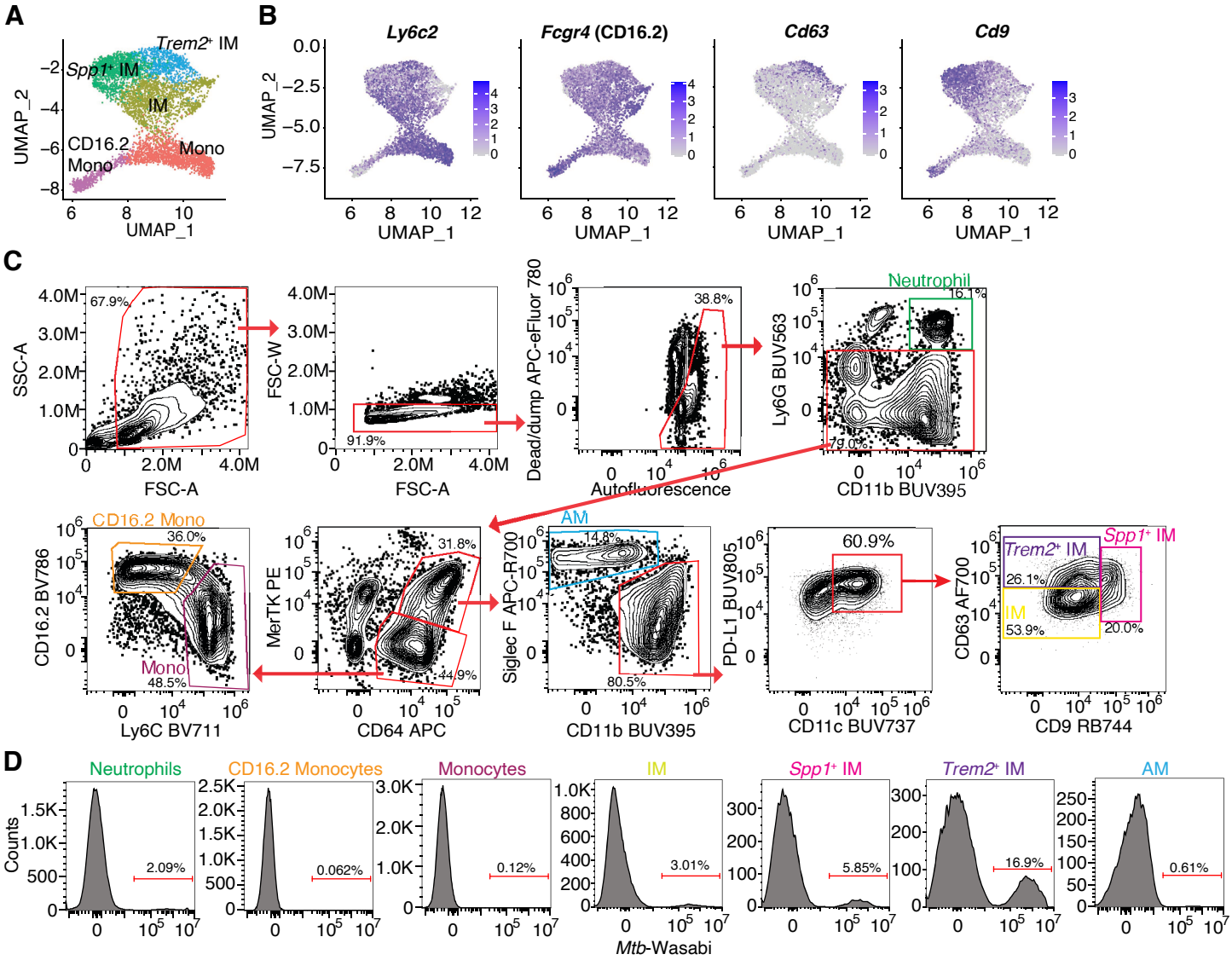

Supplementary Figure 6.

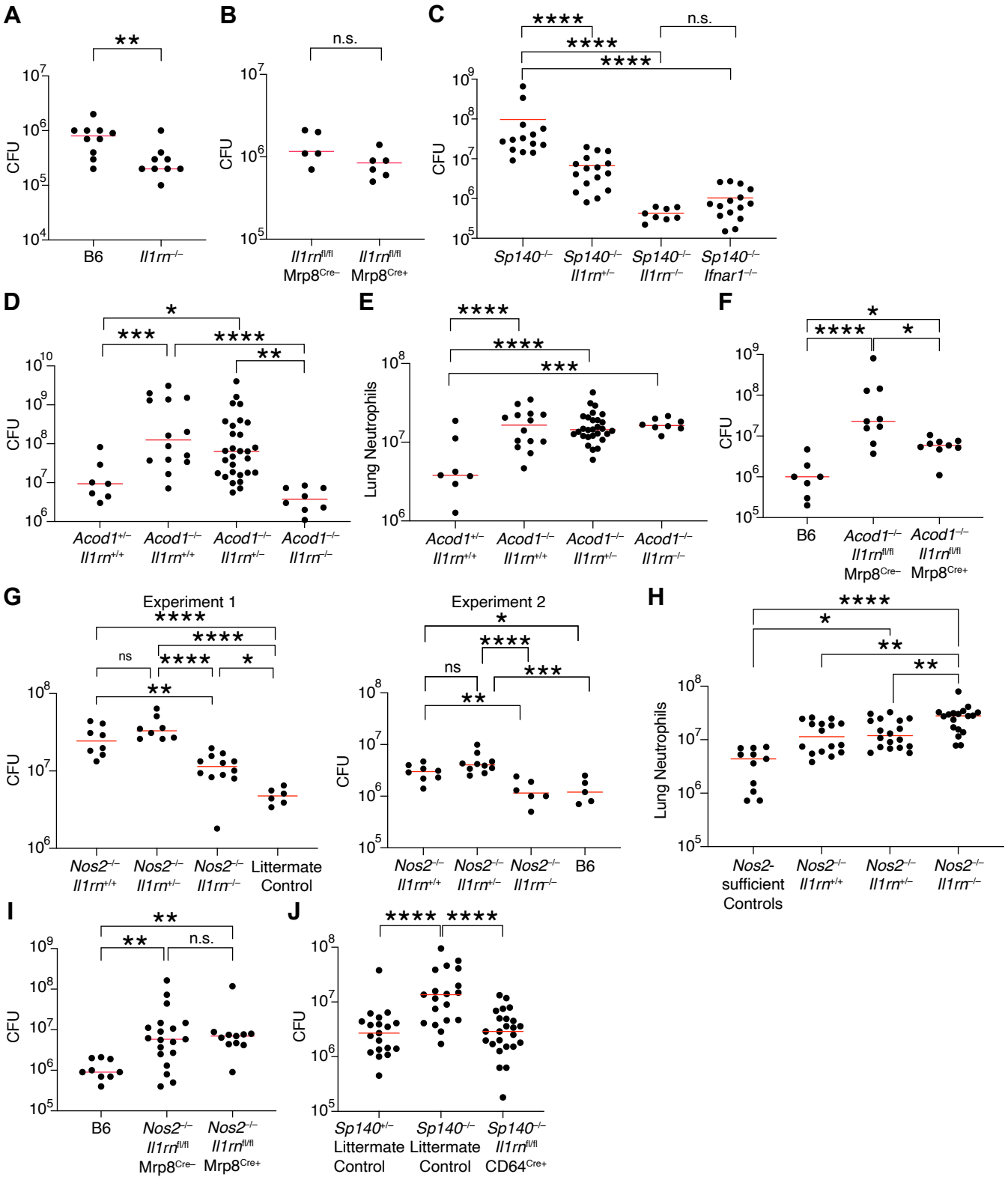

Figure 5.

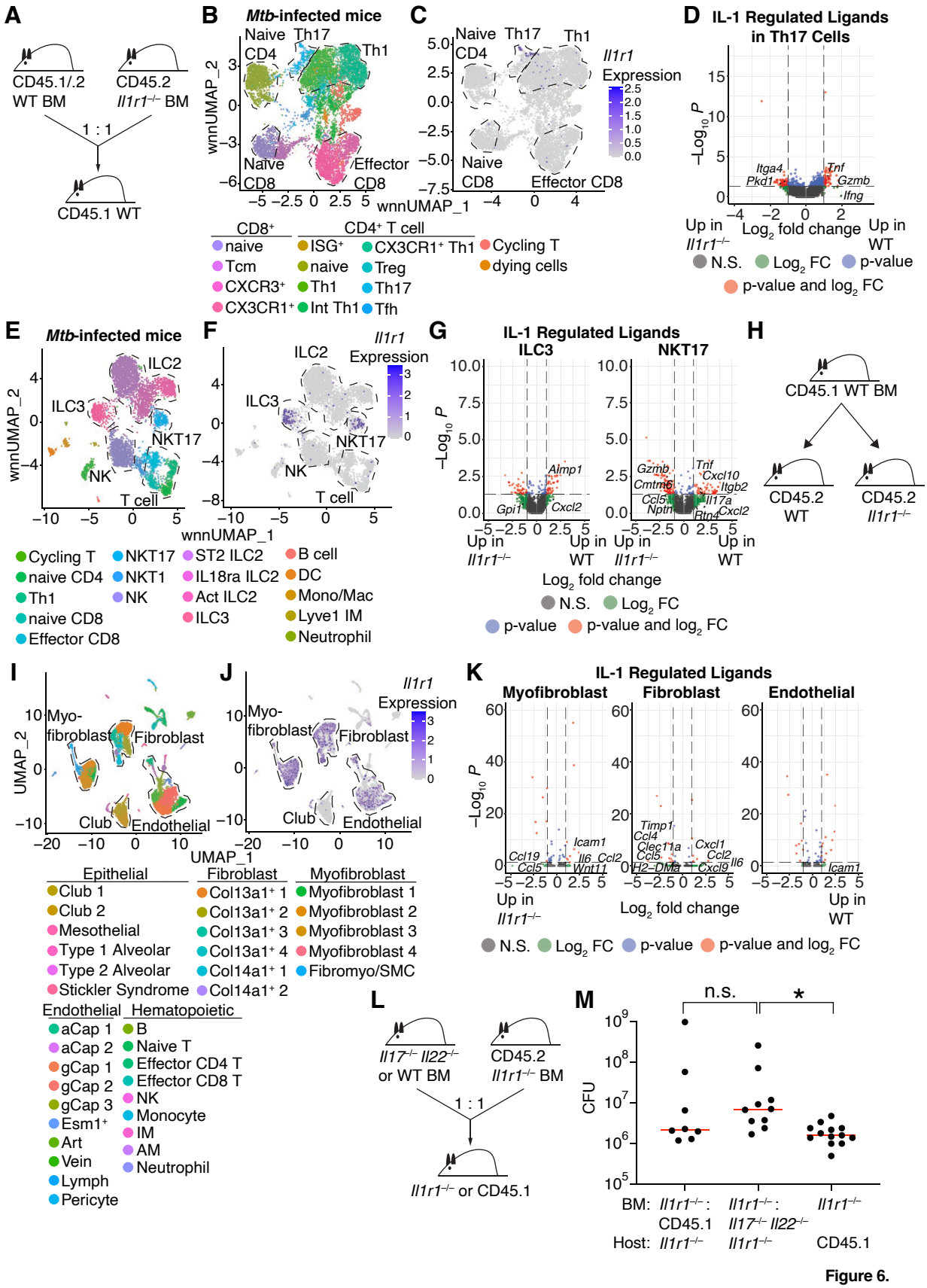

Figure 6.

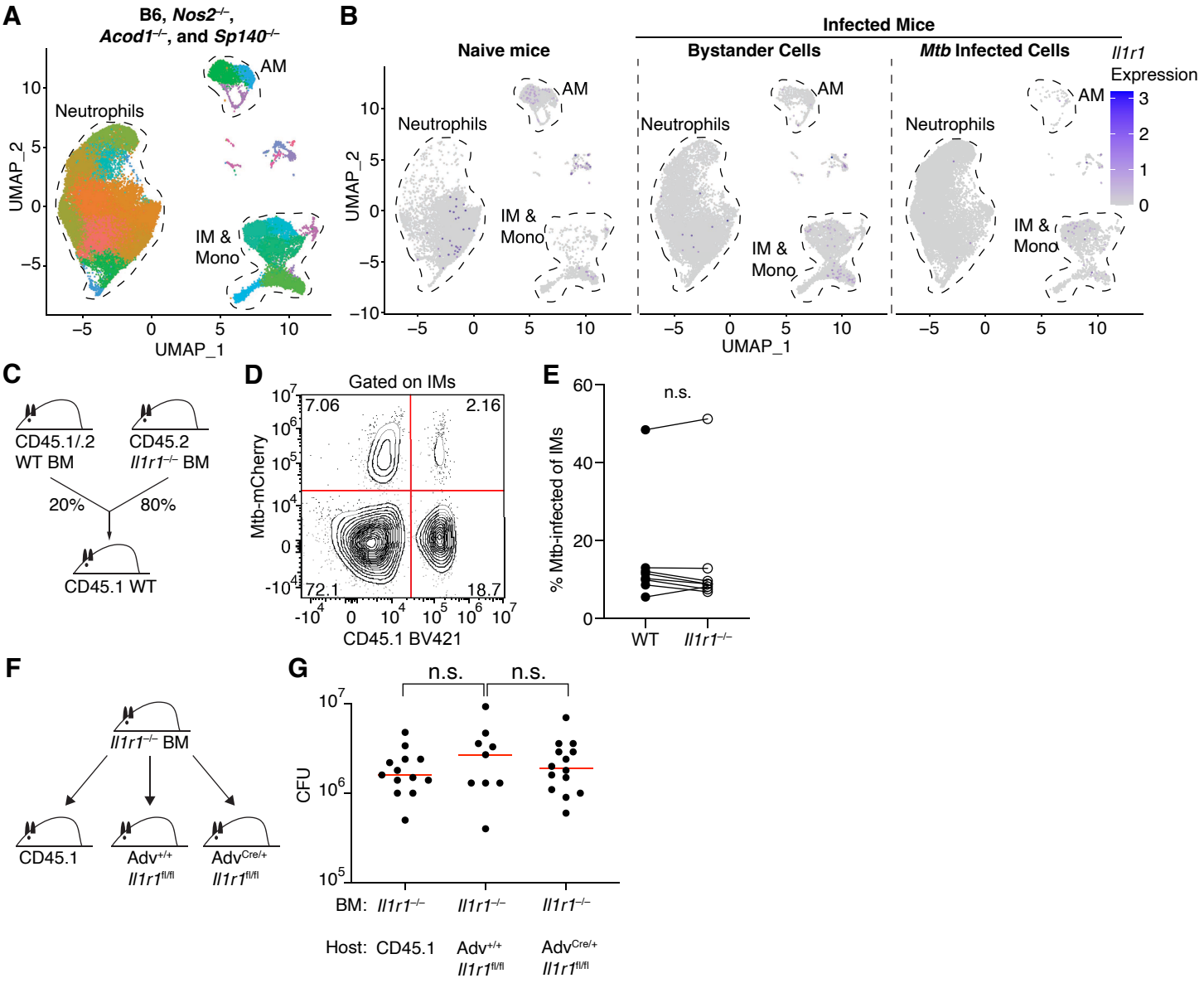

Supplementary Figure 7.

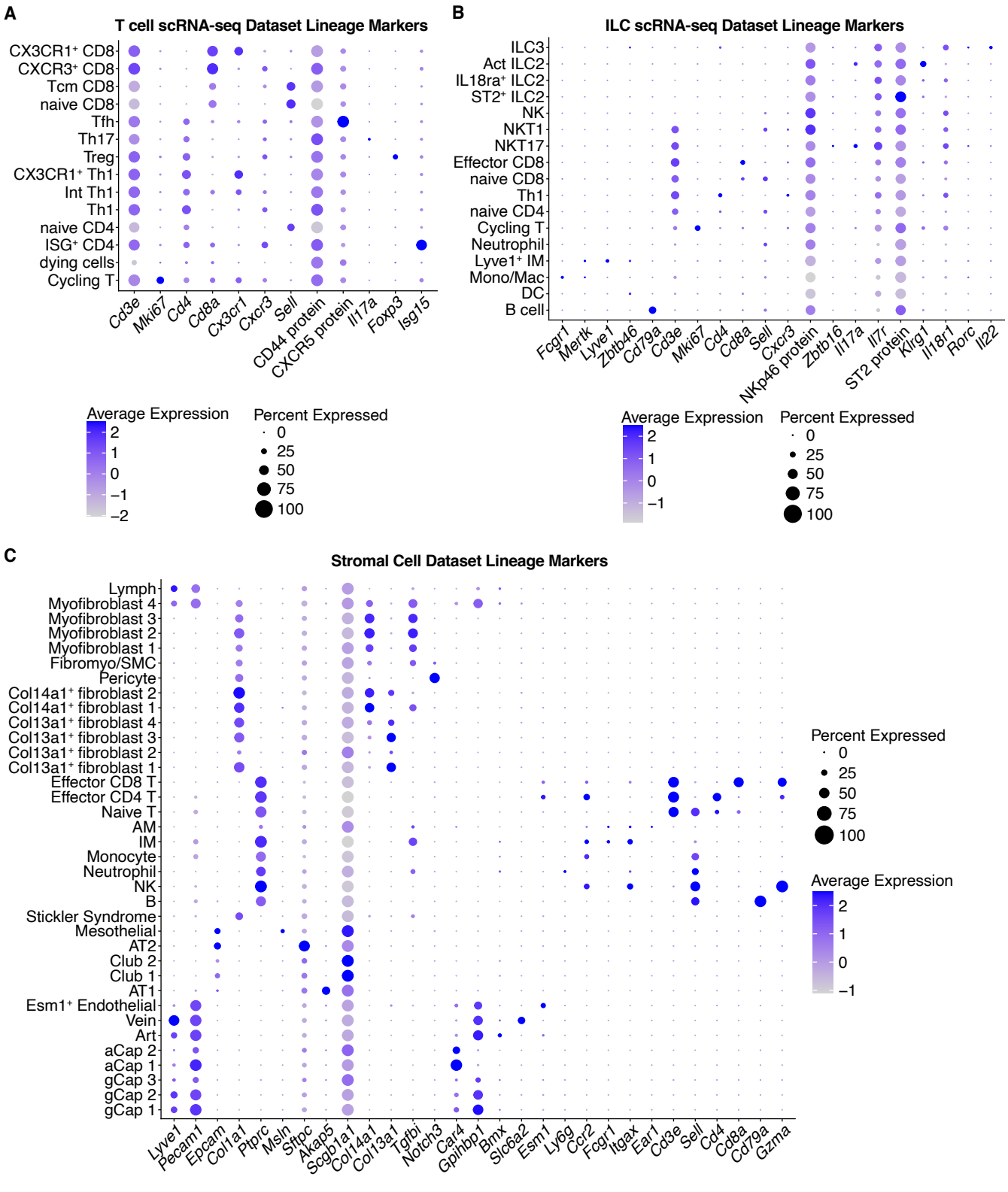

Supplementary Figure 8.

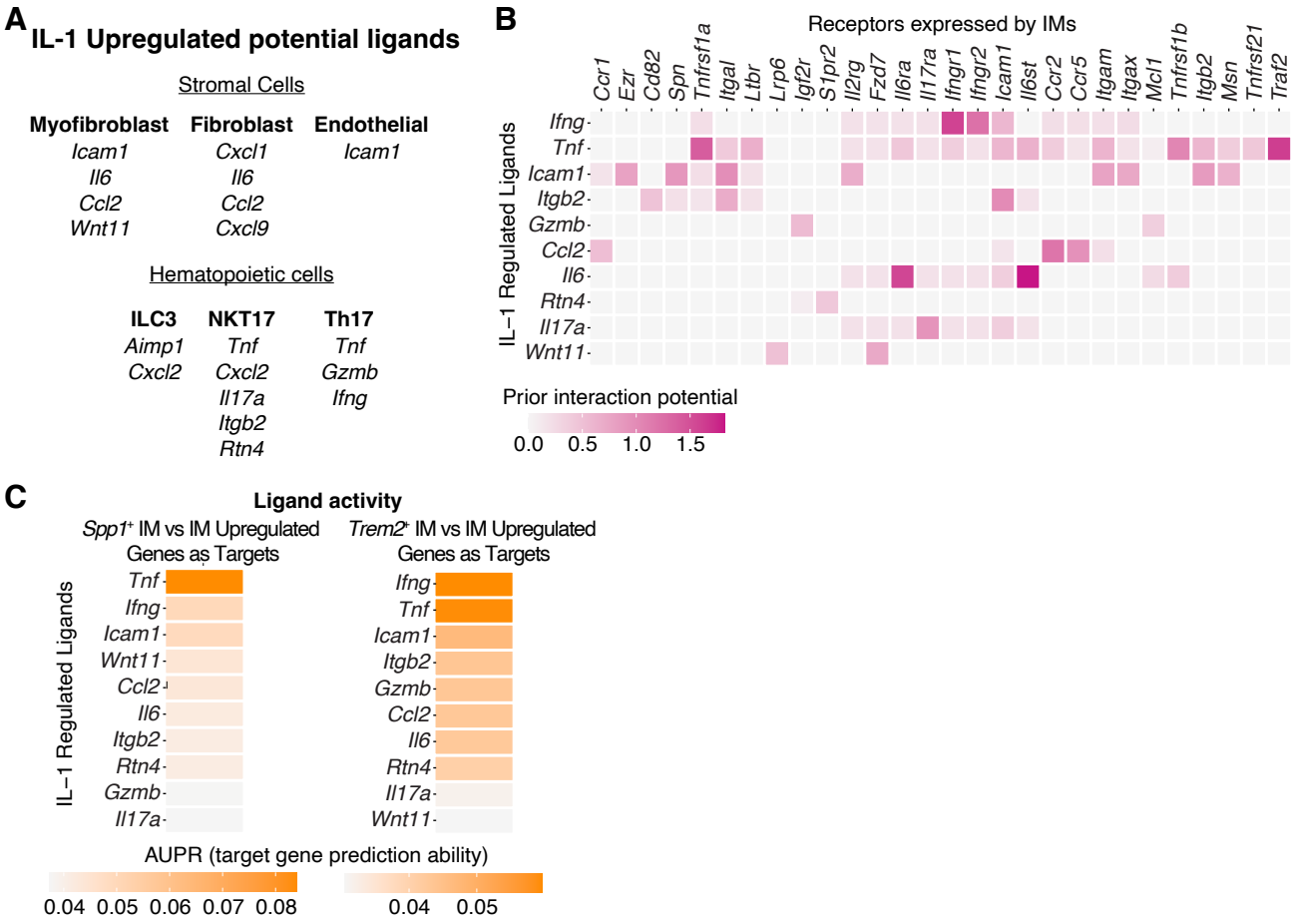

Supplementary Figure 9.